STRUCTURE-PERFORMANCE CORRELATION IN ROCK-SALT AND SPINEL HIGH ENTROPY OXIDES FOR OXYGEN ELECTROCATALYSIS AND PSEUDOCAPACITIVE ENERGY STORAGE

A THESIS SUBMITTED TO
THE GRADUATE SCHOOL OF NATURAL AND APPLIED SCIENCES
OF
MIDDLE EAST TECHNICAL UNIVERSITY

BY

ALİ BURÇAY COŞKUNER

IN PARTIAL FULFILLMENT OF THE REQUIREMENTS
FOR
THE DEGREE OF MASTER OF SCIENCE
IN
METALLURGICAL AND MATERIALS ENGINEERING

SEPTEMBER 2025

Approval of the thesis:

STRUCTURE-PERFORMANCE CORRELATION IN ROCK-SALT AND SPINEL HIGH ENTROPY OXIDES FOR OXYGEN ELECTROCATALYSIS AND PSEUDOCAPACITIVE ENERGY STORAGE

submitted by **ALİ BURÇAY COŞKUNER** in partial fulfillment of the requirements for the degree of **Master of Science in Metallurgical and Materials Engineering, Middle East Technical University** by,

Prof. Dr. Naci Emre Altun
Dean, **Graduate School of Natural and Applied Sciences** ________________

Prof. Dr. Mehmet Kadri Aydınol
Head of the Department, **Metallurgical and Materials Engineering** ________________

Assoc. Prof. Çiğdem Toparlı
Supervisor, **Metallurgical and Materials Engineering, METU** ________________

Examining Committee Members:

Prof. Dr. Mehmet Kadri Aydınol
Metallurgical and Materials Eng, METU ________________

Assoc. Prof. Çiğdem Toparlı
Metallurgical and Materials Eng, METU ________________

Prof. Dr. Hüsnü Emrah Ünalan
Metallurgical and Materials Eng, METU ________________

Assoc. Prof. Burak Ülgüt
Chemistry, Bilkent Uni. ________________

Assoc. Prof. Gökhan Çelik
Chemical Engineering, METU ________________

Date: 01.09.2025

I hereby declare that all information in this document has been obtained and presented in accordance with academic rules and ethical conduct. I also declare that, as required by these rules and conduct, I have fully cited and referenced all material and results that are not original to this work.

Name Last name: Ali Burçay Coşkuner

Signature :

ABSTRACT

STRUCTURE-PERFORMANCE CORRELATION IN ROCK-SALT AND SPINEL HIGH ENTROPY OXIDES FOR OXYGEN ELECTROCATALYSIS AND PSEUDOCAPACITIVE ENERGY STORAGE

Coşkuner, Ali Burçay
Master of Science, Metallurgical and Materials Engineering
Supervisor: Assoc. Prof. Çiğdem Toparlı

September 2025, 77 pages

Electrochemical energy materials are increasingly important for enabling clean energy conversion and storage. Depending on the process mechanism, these materials can function as either electrocatalysts or electrodes. A clear understanding of their structural characteristics is essential for tailoring electrochemical behavior and achieving high-performance devices.

In this study, the influence of crystal structure on the oxygen electrocatalysis and capacitive electrode performance of high-entropy oxides (HEOs) was investigated. Two HEOs with distinct crystal structures, rock-salt (HRS) and spinel cubic (HSP), were synthesized. For the oxygen evolution reaction (OER), the overpotentials at a current density of 10 mA cm^{-2} were 311 mV for HRS and 357 mV for HSP. In zinc–air battery (ZnAB) testing, the HRS-based cell sustained stable operation for nearly 180 h, while the HSP-based cell lost stability after about 60 h. This stability difference is likely related to the microstrain in addition to the configurational entropy, which is expected to be higher in HRS. Williamson–Hall analysis confirmed that HRS likely exhibits significantly greater inhomogeneous lattice strain than HSP

when cationic sites are occupied by Ni, Co, Cr, Cu, and Al, reflecting structural differences. In capacitive performance tests, specific capacities at 0.5 A g^{-1} were 307 F g^{-1} for HRS and 166 F g^{-1} for HSP. Electrochemical analysis further revealed that HRS behaves as a pseudocapacitive electrode, whereas HSP displays characteristics of a battery-type electrode.

Keywords: High Entropy Oxide, Crystal Structure, Electrocatalysis, Zinc-air Battery, Supercapacitor.

ÖZ

OKSİJEN ELEKTROKATALİZİ VE KAPASİTÖR-BENZERİ ENERJİ DEPOLAMA SÜREÇLERİ İÇİN KAYA TUZU VE SPİNEL GRUBU YÜKSEK ENTROPİLİ OKSİTLERİN KRİSTAL YAPI-PERFORMANS İLİŞKİSİ

Coşkuner, Ali Burçay
Yüksek Lisans, Metalurji ve Malzeme Mühendisliği
Tez Yöneticisi: Assist. Prof. Çiğdem Toparlı

Eylül 2025, 77 sayfa

Elektrokimyasal enerji malzemeleri, temiz enerji dönüşümü ve depolanmasını sağlamak için giderek daha önemli hale gelmektedir. Süreç mekanizmasına bağlı olarak, bu malzemeler hem elektrokatalizör hem de elektrot olarak işlev görebilir. Elektrokimyasal davranışı uyarlamak ve yüksek performanslı cihazlar elde etmek için yapısal özelliklerin net bir şekilde anlaşılması kritik öneme sahiptir.

Bu çalışmada, yüksek entropili oksitlerin (HEO) oksijen elektrokatalizi ve kapasitif elektrot performansı üzerindeki kristal yapı etkisi araştırılmıştır. Kaya-tuzu (HRS) ve spinel kübik (HSP) kristal yapıya sahip iki farklı HEO sentezlenmiştir. Oksijen gelişim reaksiyonu (OER) için 10 mA cm^{-2} akım yoğunluğundaki aşırı potansiyeller HRS için 311 mV, HSP için ise 357 mV olarak belirlenmiştir. Çinko–hava pili (ZnAB) testlerinde HRS tabanlı hücre yaklaşık 180 saat boyunca kararlı çalışmasını sürdürürken, HSP tabanlı hücre yaklaşık 60 saat sonra kararlılığını kaybetmiştir. Bu kararlılık farkının, konfigürasyonel entropinin yanında, HRS'de daha yüksek olduğu

düşünülen kafes gerilmesinden kaynaklandığı düşünülmektedir. Williamson–Hall analizi, katyonik bölgelerin Ni, Co, Cr, Cu ve Al ile doldurulduğu durumda, HRS'nin kristal yapısındaki farklılıklar nedeniyle HSP'ye kıyasla belirgin derecede daha yüksek oranda heterojen kafes gerilmesi gösterebileceği yorumu yapılmıştır. Kapasitif performans testlerinde, 0.5 A g^{-1} akım yoğunluğunda özgül kapasiteler HRS için 307 F g^{-1}, HSP için ise 166 F g^{-1} olarak hesaplanmıştır. Elektrokimyasal analizler, HRS'nin psödokapasitif bir elektrot gibi davrandığını, HSP'nin ise pil tipi elektrot özellikleri sergilediğini göstermiştir.

Anahtar Kelimeler: Yüksek Entropili Oksit, Kristal Yapı, Elektrokataliz, Çinko-hava Bataryası. Süper kapasitör.

This thesis is dedicated to my mother and my two big brothers.

ACKNOWLEDGMENTS

I would like to express my deepest gratitude to my advisor, Assoc. Prof. Dr. Çiğdem Toparlı, for her encouraging, supportive, and insightful guidance throughout this research journey. Even during challenging times, her trust and support were invaluable, and I am truly thankful for her mentorship both academically and in shaping my career path.

I also extend my thanks to Prof. Dr. Tayfur Öztürk, Prof. Dr. Eren Kalay, Prof. Dr. Emrah Ünalan, and the late Assoc. Prof. Dr. Caner Şimşir, as well as their research groups, whose contributions greatly enriched my work.

My sincere appreciation goes to my lab colleagues Kasım Erdem Erik, Hüseyin İnan Cihan, Hasan Girgin, and Nazlıcan Uysal for their support. I am especially grateful to Tuna Dikmen and Zeynep Ilgın Yüceer for their close collaboration and assistance. I also thank Tuncay Erdil, Çağla Özgür, and Uygar Geyikçi, from whom I learned a great deal in experimental research, and my friends Cansu Aygüzer and Doğu Şeyda for their companionship during my M.S. studies.

I am indebted to my dearest friends Seyhan Ergüeloğlu, Ali Eren Ergüzoğlu, Zinarin Aktaş, İrem Pınar, Ayda Ecem Çele, Nergis Yasav, and Ömer Utku Emeç for always making me feel their friendship and support. I also thank my aunts and especially my aunt-in-law Selda Ergüzoğlu for their warm encouragement.

Finally, I owe my deepest gratitude to my precious mother Emine Coşkuner, and my brothers Yakup Berk Coşkuner and Mehmet Can Coşkuner, whose unwavering love and presence have been my greatest strength. I feel truly fortunate to have them in my life.

TABLE OF CONTENTS

LIST OF TABLES

TABLES

LIST OF FIGURES

FIGURES

CHAPTER 1

INTRODUCTION

It is essential to switch from non-renewable to renewable energy sources in areas such as transportation and industry to reduce environmental pollution and meet the growing energy demand. [1–4] Developing novel electrochemical energy storage systems is vital for enhancing the economic viability of renewable energy sources.[5] Currently, rechargeable metal-air batteries are considered among the most promising energy storage solutions.[6] Among the different types of metal-air batteries, zinc-air batteries (ZnABs) have gained attention for grid energy storage due to their high energy density, low cost because of the abundance of zinc, and safe operating features.[7] Zinc-air batteries (ZnABs) rely on the oxygen evolution reaction (OER) and the oxygen reduction reaction (ORR), which occur at the air cathode during charging and discharging, respectively. The overall performance of ZnABs is closely linked to the rate of these reactions, which typically exhibits slow kinetics. Thus, the development of efficient bifunctional electrocatalysts is essential to improve the battery performance.[8,9] In addition to ZnABs, accelerating OER/ORR is also crucial for green hydrogen production because green hydrogen is produced by a water electrolysis method that is driven by renewable energy.[10] However, currently, percentage of electrolysis application among the other methods is only 4% as seen in Fig. 1.1.[11] To design bifunctional OER/ORR electrocatalysts , the reaction mechanisms, and how these reactions are affected by the structural properties of electrocatalysts must be deeply investigated. Designing effective bifunctional OER/ORR electrocatalysts requires a thorough investigation of the reaction mechanisms and the influence of electrocatalyst structural properties on these reactions.[12]

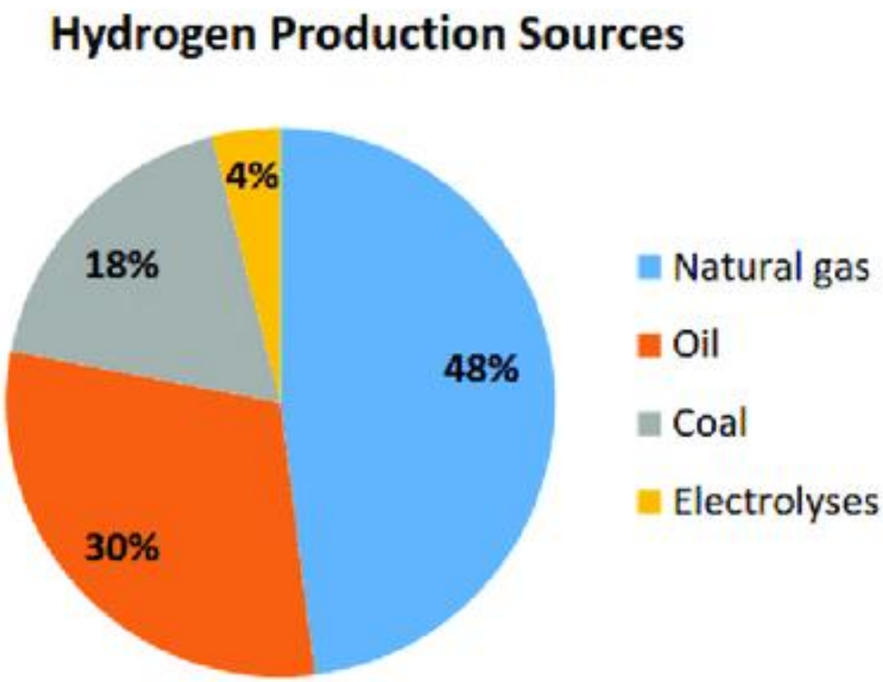

Figure 1.1 Percentages of industrial hydrogen production sources. Reproduced from [11].

With respect to these principles, electrocatalysts can be engineered by tuning various factors such as oxygen vacancies, crystal structure, electronic structure, lattice strain, chemical environment, metal–oxygen bond length, interfacial properties and morphology.[12] Currently, noble metal-based electrocatalysts like IrO_2 and Pt/C are predominantly used in commercial ZnABs. However, their high cost, limited availability, and poor long-term stability hinder large-scale production.[13] The limitations of noble metal electrocatalysts have led scientists and engineers to develop non-noble metal-based alternatives, such as high-entropy oxides[14], perovskites[15], borides[16], sulfides[17], phosphides[18], and others.[19] High-entropy oxides (HEOs) are single-phase materials composed of at least five different elements in near-equal or equal molar percentages. Their high chemical stability, attributed to the effect of entropy stabilization, makes them particularly attractive for electrocatalysis.[20] Especially, HEOs including 3d transition metals such as Ni, Co, Fe, Zn, Cu, Cr, and Mn in the cationic sites have demonstrated impressive electrocatalytic performance for OER and ORR, primarily due to their tunable electronic structures.[21] Another promising application of HEOs is in supercapacitors, particularly as pseudocapacitive energy storage materials.[22] Pseudocapacitors are becoming more attractive for energy research because of it location in an intermediate region between devices with high power densities and high energy densities, namely capacitors and batteries. They have higher energy densities compared to conventional capacitors, and higher power densities compared to batteries. In other words, they bridge the gap between batteries and traditional electrostatic capacitors. These properties coupled with their good cyclic performance and safe operation enable them to be used for effectively storing the energy harnessed from renewable sources.[23–25]

The present thesis study investigates characteristics of two different structured HEOs for both ZnAB and supercapacitor applications, and how crystal structure is related to electrochemical performance in these devices. A HEO with a rock-salt structure (HRS) is investigated for ZnAB and supercapacitor applications for the first time, and its electrochemical performance is compared with that of its spinel-structured counterpart (HSP) composed of the same elements. Both HEOs were synthesized by sol-gel Pechini method with equiatomic cationic sites with Ni, Co, Cr, Cu, Al metals. Unlike heat treatment under air environment in the syntesis of HSP, hydrogen environment preferred for HRS synthesis[26], on the other hand, HSP was treated under an air environment. The electrocatalysts were evaluated for their electrocatalytic OER/ORR performance, activity and stability, and subsequently tested in a ZnAB cell to examine device performance. The HEO possessing a rock-salt crystal structure demonstrates enhanced OER electrocatalytic activity compared to its spinel cubic counterpart, characterized by a lower overpotential at a current density of 10 mA cm^{-2}, accelerated reaction kinetics, improved charge transfer efficiency, and superior intrinsic activity. Notably, the ZnAB assembled using the rock-salt structured HEO exhibits significantly better cyclic charge-discharge stability, operating steadily for nearly 180 hours, whereas the battery employing spinel cubic structured HEO loses its cycling stability after only 60 hours of operation. In addition to electrocatalysis research, HRS and HSP also examined as electrode materials for supercapacitors. Specific capacities with three-electrode experiments were calculated at $0.5\ Ag^{-1}$ as $307\ Fg^{-1}$ and $166\ Fg^{-1}$ for HRS and HSP, respectively. Electrochemical experiments verified that HRS can be classified as pseudocapacitive type electrode material whereas HSP is battery-type electrode material. In terms of their cyclic durability, both HEOs exhibit approximately 95% capacity retention after 1000 cycles.

CHAPTER 2

LITERATURE REVIEW

2.1 Oxygen Electrocatalysis

Electrocatalysts are materials that accelerate electrochemical processes and ideally enhance the selectivity of these processes toward the desired product.[27] Since electrochemical processes are generally free from greenhouse gas emissions, they have become attractive to researchers focusing on sustainable technologies for the energy and chemical industries.[28] The most extensively studied electrocatalytic processes include water splitting, ammonia synthesis, CO_2 reduction, and biomass valorization, all aimed at improving economic feasibility and environmental sustainability.[29] Noble metal-based materials have been widely investigated due to their high catalytic activity; however, they often fail to meet the cost-effectiveness requirements of electrochemical technologies.[30] Consequently, transition metal-based catalysts are gaining attention because of their natural abundance and lower cost.[31] Oxygen evolution and reduction reactions are particularly important, as their sluggish kinetics limit the performance of technologies such as water electrolyzers, fuel cells, and metal–air batteries.[32] As a result, oxygen electrocatalysis has emerged as one of the most significant branches of electrocatalyst research.[33]

In the case of oxygen electrocatalysis, the performance of water electrolyzers and fuel cells depends exclusively on the oxygen evolution reaction (OER) and the oxygen reduction reaction (ORR), respectively.[34,35] In contrast, the operation of metal–air batteries relies on both OER and ORR; therefore, bifunctional electrocatalysts are required at the air cathode opposite the metal anode, such as zinc or lithium.[36]

2.1.1 Oxygen Evolution Reaction (OER)

The oxygen evolution reaction (OER), as written in Eq. (1) for alkaline environment, occurs on the anode side of water electrolysis, coupled with the hydrogen evolution reaction (HER) at the cathode.[37] OER also takes place at the air cathode of a metal–air battery, where the anode is composed of a metal such as zinc, iron, or aluminum. [38]

$$4OH^- \rightarrow O_{2(g)} + 2H_2O_{(l)} + 4e^- \tag{1}$$

The mechanism of OER in the alkaline electrolyte composed of four elementary steps usually, named as adsorbate evolution mechanism, AEM, shown in Eq. (2-5).[39] Asterisk written in the equations represent catalytic active site, and species with asterisk sign indicates adsorption of the corresponding species.

$$* + OH^- \rightarrow *OH + e^- \tag{2}$$

$$*OH + OH^- \rightarrow *O + H_2O_{(l)} + e^- \tag{3}$$

$$*O + OH^- \rightarrow *OOH + e^- \tag{4}$$

$$*OOH^- + OH^- \rightarrow * + O_{2(g)} + H_2O_{(l)} + e^- \tag{5}$$

As seen from the above equations, the adsorption of oxygen intermediates plays a critical role in determining catalytic activity. When these intermediates bind too strongly to the active sites, the desorption of products becomes hindered. Conversely, if the adsorption is too weak, intermediates desorb too easily, preventing sufficient interaction of reactants to form the desired products. Therefore, achieving an optimal level of intermediate adsorption is essential to maximize catalytic activity according to the Sabatier principle.[40] Another widely discussed pathway for OER is the lattice oxygen mechanism (LOM). The working principle of this mechanism is based on the participation of lattice oxygen.[41] Mentioned OER mechanisms can be summarized as illustrated in Fig. 2.1a and Fig. 2.1b for AEM and LOM, respectively.[42]

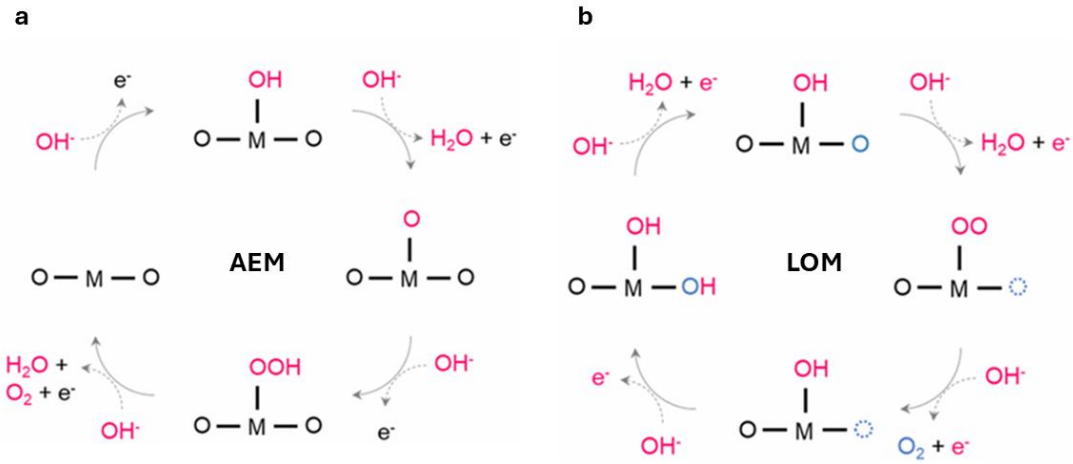

Figure 2.1 Representations of (a) AEM and (b) LOM, reproduced from [42].

According to a density functional theory (DFT) study on oxygen electrocatalysts, LOM-driven catalysts demonstrate superior activity for OER compared to AEM, in agreement with earlier reports in the literature; however, the study have mentioned that LOM-driven catalysts might not work reversibly for a long-time due to the tendency of corrosion and amorphization.[43] Another study also discussed that LOM pathway leads to instability of the catalyst surface.[42] LOM and AEM are two competing mechanisms that often occur simultaneously on the electrocatalyst surface. The presence of oxygen vacancies can convert part of the AEM pathway into LOM, thereby enhancing OER activity. However, this transformation may also lead to metal dissolution and structural instability. Therefore, regulating the trade-off between AEM and LOM is essential to balance catalytic activity with durability, ultimately yielding a more efficient and stable catalyst.[44]

2.1.2 Oxygen Reduction Reaction (ORR)

The oxygen reduction reaction (ORR) has numerous applications in electrochemical technologies, ranging from chemical synthesis to energy conversion. ORR pathways can be classified based on whether oxygen gas (O_2) is reduced completely or only partially[45]. Both ORR pathways can proceed in either alkaline or acidic electrolytes; however, this study focuses on the alkaline environment.[45] As shown in Eq. (6), the partial reduction of O_2 produces peroxide ions (HO_2^-), which is valuable for peroxide synthesis.[46]

$$O_{2(g)} + H_2O_{(l)} + 2e^- \rightarrow HO_2^- + OH^- \quad (6)$$

$$HO_2^- + H_2O_{(l)} + 2e^- \rightarrow 3OH^- \quad (7)$$

$$O_{2(g)} + 2H_2O_{(l)} + 4e^- \rightarrow 4OH^- \quad (8)$$

In contrast, further reduction of peroxide ions, as represented in Eq. (7), leads to hydroxide ions (OH^-).[47] This complete reduction pathway as shown in Eq. (8), is more relevant for energy conversion processes than for chemical synthesis. The performance of ORR is therefore a key factor in determining the efficiency of devices such as metal–air batteries and fuel cells.[48,49] In summary, the two-electron ORR pathway is desirable for peroxide synthesis, whereas the four-electron pathway is essential for energy conversion devices.

2.1.3 Zinc-air Battery

Although nowadays, lithium-ion batteries have the highest performance among the other battery technologies, metal-air batteries arise as a rival due to the safety requirements for energy storage.[50] Metal-air batteries mostly use earth abundant metals, like Zn, Al, and Fe, as anode material placing the technology more sustainable.[50] The cathode side of the battery is called air-cathode due to its openness to the atmosphere to use O_2 from the ambient air. Presence of the air cathode reduces the weight of a battery significantly improves the energy density.[50] Corresponding battery reactions for a zinc-air battery are presented in Eqs (9-12).

Reactions at Zn anode: $$Zn + 4OH^- \leftrightarrow Zn(OH)_4^{2-} + 2e^- \quad (9)$$

$$Zn(OH)_4^{2-} \leftrightarrow ZnO + 2OH^- + H_2O \quad (10)$$

Reactions at air cathode: $O_2 + 2H_2O + 4e^- \leftrightarrow 4OH^-$ (11)

Overall Zn-air cell reaction: $2Zn + O_2 \leftrightarrow 2ZnO$ (12)

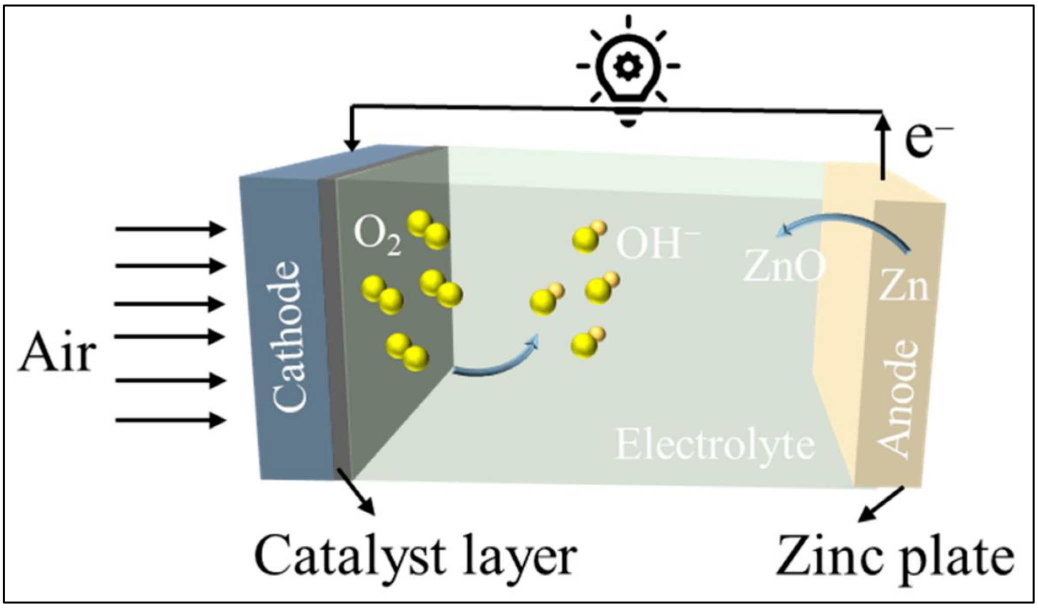

Figure 2.2 Representative Zn-air battery cell, reproduced from[51].

Among the other metal-air batteries zinc-air batteries take more attention these days, due to their safety[52], eco-friendliness[53], low cost with high capacity[54], maturity[55], and practicality[56]. However, it faces various challenges about battery chemistry to overcome. Zinc–air batteries suffer from zinc dendrite growth, hydrogen evolution (HER), and ZnO passivation, which lower coulombic efficiency and shorten cycle life.[55] Zinc anode faces self-corrosion and morphological instability during cycling.[57] Because of the environmental sensitivity of the air cathode and electrolyte, KOH, performance is strongly affected by humidity, temperature, and CO_2 uptake poisoning the electrolyte, which forms carbonates that reduce electrolyte conductivity.[58] Electrolyte poisoning via CO_2 uptake and parasitic HER can be seen in Eqs. (13-15).

$KOH + CO_2 \rightarrow KHCO_3$ (13)

$2KOH + CO_2 \rightarrow K_2CO_3 + H_2O$ (14)

$$Zn + 2H_2O + Zn(OH)_2 + H_2 \quad (15)$$

According to the classification of energy storage and conversion devices, metal-air batteries are called hybrid devices because they include metal anode, like batteries, and air cathode, as in fuel cells.[59] Ragone plot, illustrating the energy and power density characteristics of the energy storage devices, is represented in the following Fig. 2.3, to visualize the position of zinc-air batteries.

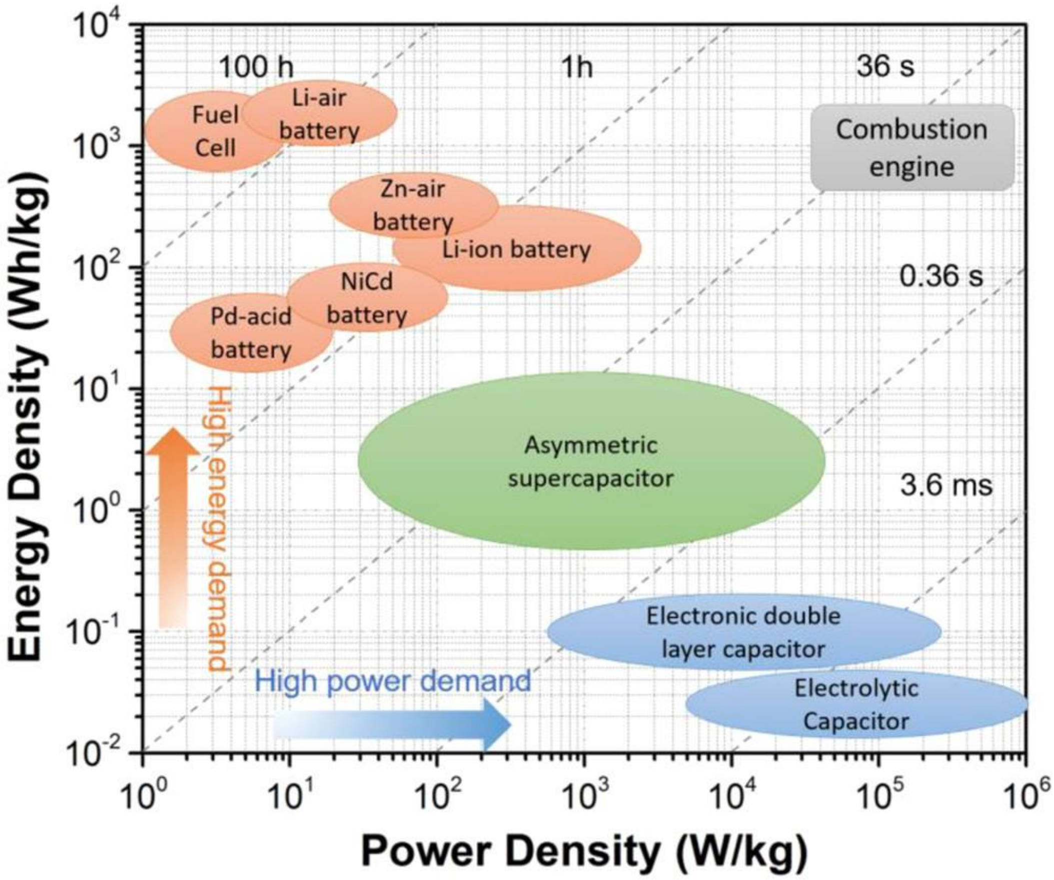

Figure 2.3 Ragone plot for various energy storage devices, reproduced from[60].

2.2 Pseudocapacitive Energy Storage

The most primitive capacitive process in electronics is well-known parallel plate capacitors having two conductor parallel plates separated by vacuum or a dielectric material with a certain spacing. Capacitance formula of parallel capacitors is as written in Eq. (16).[61] Where ϵ is permittivity of the dielectric material or vacuum space, A is the area of the plate, and d is the distance of the space filled with dielectric material or vacuum separating two plates from each other.

$$C = \frac{\epsilon \times A}{d} \tag{16}$$

As observed from the formula, capacitance increases with decreasing distance and increasing surface area.

Parallel plate capacitors exhibit in order of pF to μF capacitance values due to the limited surface area and distance. The idea of supercapacitor overcomes these restrictions firstly, by ideally polarizing charges in the electrolyte solution and the electrode called electrical double layer at the interface. Creation of this electrical double layer decreases the distance between the opposite charges is generally at nm level; hence, the capacitance values spike up to even F scale.[62,63] Capacitors relying on this principle are called electrical double-layer capacitors (EDLCs).[64]

The other supercapacitor category is named pseudocapacitor storing charges by also surface-controlled faradaic reactions in addition to EDLC mechanism. In surface redox pseudocapacitance, only the accessible surface and near-surface metal sites are actively involved in the redox reactions. This type of pseudocapacitive behavior is the most frequently encountered mechanism, and many materials showing this characteristic have been reported to deliver energy densities up to two orders of magnitude greater than those of electric double-layer capacitors (EDLCs). Nevertheless, the power density associated with surface redox pseudocapacitance is generally lower than that of EDLCs. This limitation arises because redox processes proceed more slowly than the electrostatic adsorption–desorption mechanism, and their kinetics are further constrained by mass-transport limitations inherent in faradaic reactions.[65] Capacitive electrodes and their electrochemical characteristics can be summarized as illustrated in Fig. 2.4.[66]

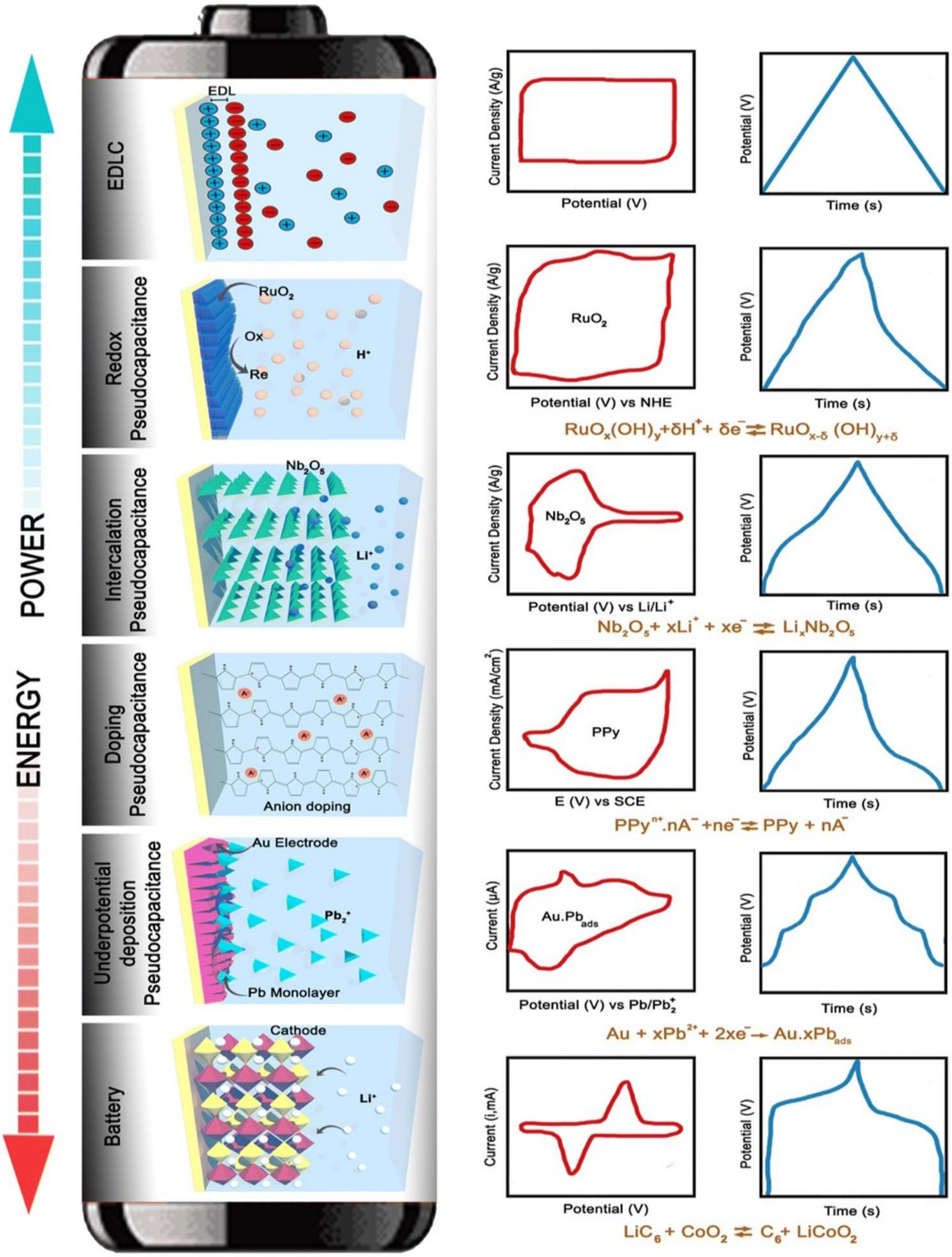

Figure 2.4 Charge storage mechanisms and their electrochemical characteristics of supercapacitor electrode materials. Reproduced from [66]

2.2.1 Charge Storage Mechanism

Charge storage mechanisms of non-EDLC electrodes are based on pseudocapacitance, surface-redox reactions, and battery-like behavior, bulk-redox reactions.[67,68] Co_3O_4[69], $MnCo_2O_4$, and $NiCo_2O_4$ are the spinel structures that exhibits battery-like behavior since oxyhydroxides are formed during charge-discharge process which indicate that charge storage rely on phase transition like batteries.[70] Battery-type phase transformation equation from spinel oxides to oxyhydroxides is represented in Eq. (17) as follows.[70]

$$M_3O_4 + OH^- + H_2O \leftrightarrow 3MOOH + e^- \quad (17)$$

On the other hand, pseudocapacitive-type electrodes predominantly exhibit reversible redox reactions (Faradaic processes) at the surface or near the surface. This pseudocapacitive nature conceptualized as reversible electrochemical adsorption of species, like OH^- ions, onto electrode surface, as represented by Eq. (18).[68]

$$M + S^+ + e^- \leftrightarrow MS_{ads} \quad (18)$$

In a KOH environment, intercalation-based pseudocapacitive behavior occurs in two steps: first, OH^- ions are adsorbed onto the active sites of the electrode surface; then, if the oxide lattice contains a large number of oxygen vacancies, O^{2-} ions can further intercalate into the bulk material.[71] In supercapacitor application the O^{2-} intercalation mechanism was studied for a perovskite oxide, $La_{0.7}Sr_{1.2}Fe_{0.9}Co_{0.1}O_4$, in a 2 M KOH electrolyte, moreover, the study reported that the increased diffusion rate of O^{2-} ions was due to the higher concentration of oxygen vacancies.[72] Cyclic voltammetry (CV) and galvanostatic charge–discharge (GCD) tests with three-electrode setup provide several clues to identify the charge storage mechanism of an electrode material.[73] A power law relation, as shown in Eq. (19), is used to determine whether the charge storage mechanism in electrode materials is surface-controlled, diffusion-controlled, or a combination of both by using CV results in several scan rates.[74]

$$i = a \times \upsilon^{b} \tag{19}$$

If the b-value is close to 0.5, the charge storage mechanism is dominated by diffusion. On the other hand, the b-value around 1 indicates surface-controlled pseudocapacitive or EDLC behavior on the electrode. When the calculated b-value is between 0.8 and 1.0, it suggests that surface processes dominate over diffusion, unlike in battery-type materials.[74] As reported in the literature, a decrease in particle or crystallite size leads to an increased contribution from capacitive, surface-controlled charge storage, rather than battery-type, diffusion-controlled mechanisms.[75] In the case of GCD, if the resulting curves exhibit a clear potential plateau around a certain voltage during discharge, this indicates that the working electrode operates via a battery-type diffusion-controlled mechanism.[76] The observed plateau potential corresponds to the redox peaks in the CV curve, if such peaks are present.[77]

2.2.2 Supercapacitor Devices

Supercapacitors are usually divided into three classes with respect to their charge storage mechanism. Electrical Double Layer Capacitors (EDLC's), rely on electrostatic charge separation for energy storage. Pseudocapactiors, rely on reversible and fast redox reactions at electrodes' surfaces. The third and final class are Hybrid Supercapacitors which contain the supercapacitors having both capacitive-type and battery-type mechanisms for energy storage at their separate electrodes.[67,78,79]

As seen from the Ragone plot provided in Fig. 2.3, asymmetric supercapacitors are located at the optimum-like position in terms of both energy and power densities. Asymmetric supercapacitors contain anode and cathode with different electrode materials different in their charge storage nature. Therefore, they are useful to design specific to the application. In sustainable energy applications, fluctuations in power generation can cause voltage flickers, which may damage sensitive electronics. Supercapacitors help suppress these instabilities by providing rapid charge–discharge capability, ensuring smoother power delivery and temporary energy storage.[80] Great power density of supercapacitors enables these devices one of the candidates to be used in electric vehicles.[81] However, supercapacitors are not sufficient in terms of energy density and need to be improved more to compete with other devices.[82] Therefore, one of the widely suggested scenarios for using supercapacitors is combining them with other energy storage devices in the same circuitry either connecting parallelly or serially. [83] Combinations of supercapacitors with batteries, fuel cells, and other storage devices are especially recommended for electric vehicles, renewable energy systems, and grid stabilization, as they balance high energy density with high power capability.[84]

2.3 HEOs as Electrocatalysts and Electrode Materials

To develop non-noble metal-based materials with thermodynamic stability comparable to noble metals, the high-entropy concept can be applied to catalyst design. according to the Gibbs free energy relation, G=H-TS, an increase in the TS term reduces the overall free energy.[85] A material is classified as a high-entropy material if its configurational entropy, as given in Eq. (20), exceeds 1.5R, where R is the gas constant.[86]

$$\Delta S_{conf} = -R \sum_{i=1}^{n} x_i ln x_i \tag{20}$$

As shown in Eq. (20), configurational entropy is expressed as a function of the molar compositions of each constituent at constant temperature and pressure. Therefore, entropy can be considered a multivariable function, as defined in Eq. (24). To determine the maximum configurational entropy, the maximum of the ΔS_{conf} function is obtained by setting the first partial derivative with respect to each independent variable equal to zero. As shown in Eqs. (21-24), the configurational entropy of the n-component system has (n-1) independent variables at constant temperature and pressure.

$$x_1 + x_2 + \cdots + x_{n-1} + x_n = 1 \tag{21}$$

$$x_n = 1 - [x_1 + x_2 + \cdots + x_{n-1}] \tag{22}$$

$$\Delta S_{conf} = -R \times (x_1 ln x_1 + x_2 ln x_2 + \cdots + x_{n-1} ln x_{n-1} + (1 - [x_1 + x_2 + \cdots + x_{n-1}]) \times ln(1 - [x_1 + x_2 + \cdots + x_{n-1}])) \tag{23}$$

$$\Delta S_{conf} = \Delta S_{conf}(x_1, x_2, x_3, \dots, x_{n-1}) \tag{24}$$

To find the molar compositions that maximize the configurational entropy, the first derivatives are written and set equal to zero for each variable as in Eqs. (25-28).

$$\frac{\partial \Delta S_{conf}}{\partial x_1} = \frac{\partial \Delta S_{conf}}{\partial x_2} = \cdots = \frac{\partial \Delta S_{conf}}{\partial x_{n-1}} = 0 \tag{25}$$

$$\frac{\partial \Delta S_{conf}}{\partial x_1} = -R \times \left(1 + ln x_1 + (-1) \times ln(1 - [x_1 + x_2 + \cdots + x_{n-1}]) + (-1) \times \frac{1-[x_1+x_2+\cdots+x_{n-1}]}{1-[x_1+x_2+\cdots+x_{n-1}]}\right) = 0 \tag{26}$$

$$\frac{\partial \Delta S_{conf}}{\partial x_1} = -R \times ln\left(\frac{x_1}{1-[x_1+x_2+\cdots+x_{n-1}]}\right) = 0 \tag{27}$$

$$x_1 = 1 - [x_1 + x_2 + \cdots + x_{n-1}] \tag{28}$$

Repeating the same calculation for each component, the coefficient of the corresponding variable becomes 2 while the others remain 1, leading to the linear system in Eqs. (29-31).

$$2x_1 + x_2 + \cdots + x_{n-1} = 1 \tag{29}$$

$$x_1 + 2x_2 + \cdots + x_{n-1} = 1 \tag{30}$$

$$\vdots \qquad\qquad \vdots$$

$$x_1 + x_2 + \cdots + 2x_{n-1} = 1 \tag{31}$$

This system can be expressed in matrix form as Eq. (32):

$$\begin{bmatrix} 2 & 1 & 1 & \cdots & 1 \\ 1 & 2 & 1 & \cdots & 1 \\ 1 & 1 & 2 & \cdots & 1 \\ \vdots & \vdots & \vdots & \ddots & \vdots \\ 1 & 1 & 1 & \cdots & 2 \end{bmatrix} \times \begin{bmatrix} x_1 \\ x_2 \\ x_3 \\ \vdots \\ x_{n-1} \end{bmatrix} = \begin{bmatrix} 1 \\ 1 \\ 1 \\ \vdots \\ 1 \end{bmatrix} \tag{32}$$

Solving Eq. (32) for any n-component system gives equimolar compositions as written in Eq. (33).

$$x_1 = x_2 = x_3 = \cdots = x_{n-1} = \frac{1}{n} \tag{33}$$

As written in Eqs. (34-35), the second derivative is checked by differentiating the first derivative of the function, written in Eq. (27), to verify whether this critical point corresponds to a maximum or a minimum. The result is negative for all permissible compositions, confirming that the stationary point is maximum:

$$\frac{\partial^2 \Delta S_{conf}}{\partial {x_1}^2} = -R \times \frac{1-[x_1+x_2+\cdots+x_{n-1}]-(-x_1)}{(1-[x_1+x_2+\cdots+x_{n-1}])^2} \times \frac{1-[x_1+x_2+\cdots+x_{n-1}]}{x_1} \tag{34}$$

$$\frac{\partial^2 \Delta S_{conf}}{\partial {x_1}^2} = -R \times \frac{1-x_2-x_3-\cdots-x_{n-1}}{x_1 \times (1-[x_1+x_2+\cdots+x_{n-1}])} < 0 \tag{35}$$

Based on this extremum analysis, the atomic percentages of all metallic components must be equal. In other words, equiatomic occupation of the metallic sites is required to achieve maximum configurational entropy.[87] Achieving configurational entropy values exceeding 1.5R requires the presence of five or more constituent elements.[88]

The most promising high entropy materials reported in the literature include high entropy alloys and ceramics, such as oxides, nitrides, carbides, borides, and silicides.[89] The focus of the present thesis is investigating high entropy oxides with rock-salt and spinel structures amongst these materials. Many studies define high entropy oxides (HEOs) as multicomponent oxides with nearly equiatomic compositions, since their configurational entropy, S_{config}, exceeds 1.5 R. The S_{config} of the synthesized HEO is calculated using Eq. (36).[90]

$$S_{config} = -R[(\textstyle\sum_{i=1}^{n} x_i ln x_i)_{cation-site} + \left(\sum_{j=1}^{m} x_j ln x_j\right)_{anion-site}] \tag{36}$$

HEOs promise potential applications for many electrochemical energy conversion and storage practices such as electrocatalysis, fuel cells, electrolyzers, batteries, and supercapacitors due to their superior structural stability and electrochemical activity.[91] Unlike single-metal oxides, which exhibit a fixed redox potential, multi-metallic systems (HEOs) offer multiple redox-active centers, thereby enabling enhanced charge storage through various redox transitions for supercapacitor applications. [92]

2.4 Structure-Performance Correlations

2.4.1 Crystal Structure of HEOs as Electrocatalysts

In evaluating the entropy of HEOs, the influence of lattice strain must be considered to the mixing enthalpy.[93] An increase in microstrain, or lattice distortion, can lead to a corresponding improvement in the material's thermodynamic stability.[94] Properly tuned lattice strain adjusts the d-band center to an optimal level. Since the adsorption energies of OER/ORR intermediates are governed by the d-band center position, this adjustment can enhance catalytic activity.[95] Strain-engineering approaches can be classified into intrinsic and artificial types. Intrinsic strain originates from lattice mismatch, structural disorder, or distortions arising from size and morphology differences. Artificial strain, on the other hand, usually involves tensile or compressive stress imposed by rigid or flexible substrates under external mechanical force.[96] A design approach was introduced in a study where the structural framework was evaluated using the standard deviation coefficient (V_σ), a parameter describing fluctuations in lattice constants throughout the material. As defined in Eq. (37), V_σ is calculated by averaging the possible lattice parameters of unit cells, thereby representing the extent of variation present.[97]

$$V_\sigma = \frac{\sigma}{\bar{x}} = \frac{\sqrt{\sum_{i=1}^{N}(x_i - \bar{x})^2}}{\bar{x}} \tag{37}$$

It has been shown that the spinel oxide, $(MgCoNiCuZn)Fe_2O_4$, exhibits a lower standard deviation coefficient, V_σ, than the rock-salt oxide, (MgCoNiCuZn)O. The higher V_σ of the rock-salt oxide suggests greater deviations of lattice parameters from the ideal case, leading to pronounced atomic-scale strain fields. This expectation was verified using HRTEM atomic strain field mapping for both oxides. Consistent with expectations, rock-salt oxide displays stronger inhomogeneous atomic strain fields. The elevated V_σ value not only indicates substantial lattice strain but also makes the synthesis of the rock-salt phase more challenging than that of the spinel phase.[97] As stated in a study focusing on multi-metallic systems, high configurational entropy and lattice distortion due to the high atomic size mismatch of the constituents contribute the phase stability of a multi-metallic system.[98] It has been documented that as microstrain in the lattice increases, the material exhibits improved oxygen evolution reaction activity along with greater thermodynamic stability.[99] Furthermore, as part of defect engineering, regulating the concentration of surface oxygen vacancies within the lattice can improve the OER activity of an electrocatalyst by modifying its electronic structure.[100] Research on perovskite-type oxides, $ABO_{3-\delta}$, has shown that as the oxygen vacancy content (δ) rises, distortions in the lattice structure may occur.[101] Likewise, the presence of oxygen vacancies enhances the electrocatalytic activity toward the ORR.[101] Introducing oxygen vacancies can be an effective approach to enhance the bifunctional activity of electrocatalysts.[102]

2.4.2 Crystal Structure of HEOs as Electrode Materials

Nickel-Cobalt based mixed oxides with both spinel and rock-salt crystal structures, $NiCo_2O_4$ and $NiCoO_2$, have been studied in a previous work, and it was concluded that rock-salt structure, $NiCoO_2$, shows higher contributions of metal d-orbital to the bands near to the Fermi-level compared to the spinel structure, $NiCo_2O_4$. Therefore, $NiCoO_2$ exhibits better electron mobility in rapid redox reactions.[103] In a related study, $NiCoO_2$ and $NiCo_2O_4$ were first investigated using density functional theory

(DFT) calculations, and the findings were later validated through capacity measurements. First-principles DFT results revealed that the superior electrochemical behavior of $NiCoO_2$ stems from its rock-salt crystal structure, which facilitates faster OH^- adsorption and deprotonation kinetics, as well as enhanced electron donation capability, making it a more effective electrode material than the spinel-structured $NiCo_2O_4$.[104]

CHAPTER 3

EXPERIMENTAL METHODS

3.1 Materials Synthesis

The modified sol-gel Pechini method was used for the synthesis of HRS, (NiCoCrCuAl)O, and HSP, $(NiCoCrCuAl)_3O_4$, powders. In two separate beakers filled with 0.1 L of de-ionized water, equimolar amounts of $Ni(NO)_3{\cdot}6H_2O$, $Co(NO)_3{\cdot}6H_2O$, $Cr(NO)_3{\cdot}9H_2O$, $Cu(NO)_3{\cdot}3H_2O$, $Al(NO)_3{\cdot}9H_2O$ salts were dissolved. For the synthesis of HSP, Citric acid were added to the mixture as a chelating agent after the dissolution of metal salts was completed, and then acryl amide addition was done. During the synthesis, the acryl-amide/metal ratio was selected as 4.5/1, and the citric-acid/metal ratio was selected as 1.5/1. However for the synthesis of HRS, acryl amide was not added to the solution and citric acid-to-metal ratio was 1/1. Using the magnetic stirrer, the solutions were then heated to 100˚C and stirred until they became gels. After the water was evaporated, mixtures were dried in an oven at 225˚C overnight. The dried gels were comminated using mortar and pestle to prepare powder forms. For the synthesis of HRS, powders were heat treated for 2 hours under H_2 flow at 300˚C. After that, another treatment for 2 hours was performed under H_2 flow at 1000˚C consecutively. For the synthesis of HSP, treatment of the powders was performed under ambient atmosphere for 2 hours at 500˚C. An overview of the synthesis route is presented in Fig. 3.1. Additionally, Thermocalc simulations were done for both high-entropy oxides to investigate the impact of synthesis conditions on the resulting material phases, elaborating in the results and discussion chapter.

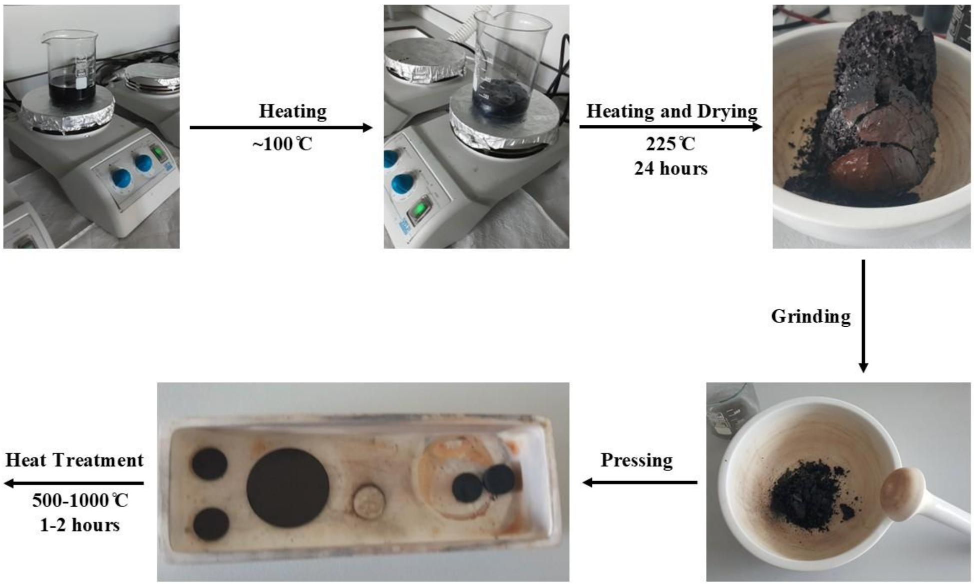

Figure 3.1 Sol-gel synthesis photos of high entropy oxides.

3.2 Structural Characterization

The characterization of the crystal structure was completed using the X-ray diffraction technique (XRD, Rigaku). XRD experiments were done between 10˚-90˚for 2θ using Cu-Kα radiation. Evaluation of the XRD results was completed by using Rietveld refinement in GSAS-II software and the calibration was done based on LaB_6 standard reference sample. Crystal structure was visualized via VESTA software. The characterization of the surface morphology was done using a scanning electron microscope (SEM) and the illustration of the elemental mappings was done using energy dispersive spectra (EDS). X-ray photoelectron spectroscopy (XPS, PHI5000VersaProbe spectrometer) was used to understand the chemical states of the elements within the material using Al-Kα radiation. The XPS peaks were examined by following the C 1 S standard spectrum of 284.6 eV. The characterization of the surface area was performed with the Brunauer-Emmett-Teller (BET) method. The amounts of the equiatomic metal cation powders were confirmed by the inductively coupled plasma optical emission spectroscopy (ICP-OES) characterization method.

3.3 Electrochemical Experiments

3.3.1 OER and ORR Performance Tests for HEOs as Electrocatalysts

Electrochemical measurements were performed using a three-electrode configuration on a rotating disk electrode (RDE, BASI), where a glassy carbon electrode was connected to a GAMRY Reference 3000 potentiostat/galvanostat/ZRA. A platinum wire served as the counter electrode, while an Ag/AgCl electrode functioned as the reference. All potentials measured against Ag/AgCl were converted to reversible hydrogen electrode (RHE) values using the Nernst equation provided in Eq. (38).

$$E[versus\ RHE] = E[versus\ Ag/AgCl] + 0.059 \times pH + 0.198 \tag{38}$$

For electrochemical tests, 0.1 M and 1 M KOH solutions were employed as electrolytes for three-electrode measurements and double-layer capacitance evaluation, respectively. The catalyst ink was prepared by combining 10 mg of active material, 5 mg of Super P carbon black, and 0.2 mL of 5 wt% Nafion solution (Sigma-Aldrich) in 2 mL of ethanol, followed by thorough grinding. The resulting mixture was sonicated to ensure uniform dispersion. A defined amount of the ink was then drop-cast onto the surface of a glassy carbon electrode to fabricate the working electrode. Linear sweep voltammetry, LSV, was carried out for both OER and ORR within the potential range of 0.20 to 1.10 V versus Ag/AgCl, using a scan rate of 10 mV s^{-1}. To evaluate the number of electrons transferred during the ORR process, LSV measurements were also performed at various rotation rates under the same potential window (0.20–1.10 V vs Ag/AgCl), but with a slower scan rate of 5 mV s^{-1}. The LSV data were processed by plotting 1/J against $1/\omega^{1/2}$ based on the Koutecky-Levich equation[105] as can be seen in Eq. (39), and the slopes of these plots were used to determine the number of electrons involved in the reaction.

$$\frac{1}{j} = \frac{1}{j_k} + \frac{1}{j_l} = \frac{1}{j_k} + \frac{1}{0.62nFD^{2/3}\omega^{1/2}\mu^{-1/6}C_0^*} \tag{39}$$

Electrochemical impedance spectroscopy, EIS, measurements were performed at a DC potential corresponding to a current density of 10 mA cm^{-2} within the OER region across a frequency range from 10^{-2} to 10^{5} Hz, using a rotating disk electrode with three-electrode configuration to evaluate the electrical conductivity of the materials. Additionally, the double-layer capacitance of the oxides was estimated by cyclic voltammetry, CV, experiments performed in the potential range of 0.20–0.30 V vs Ag/AgCl at varying scan rates in a 1 M KOH electrolyte. Representative RDE set-up can be seen in Fig. 3.2.

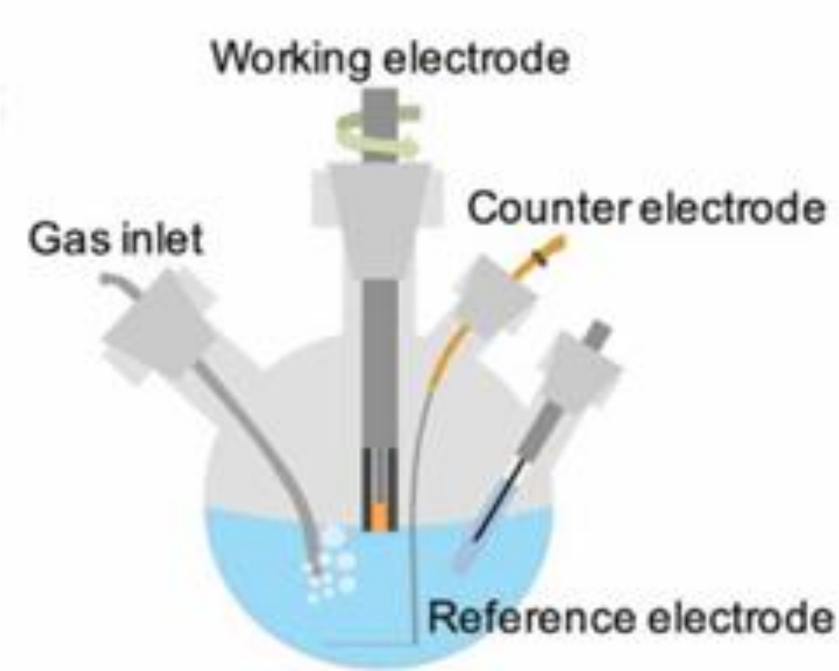

Figure 3.2 Illustration of a rotating disk electrode, reproduced from [106].

3.3.2 Capacitive Performance Tests of HEOs as Electrode Materials

A three-electrode setup, consisting of an Ag/AgCl reference electrode and a platinum wire as the auxiliary (counter) electrode, was used to evaluate the electrode materials using a GAMRY Reference 3000 potentiostat/galvanostat/ZRA. The working electrodes were prepared by coating slurries of the electroactive materials onto nickel foam substrate. The slurries were formulated by mixing the electroactive material, Super P carbon black, and PVDF binder in a weight ratio of 72/16/12 to ensure the electrical conductivity of the metal oxide electrode using N-methyl-2-pyrrolidone (NMP) as the solvent. The prepared slurry was coated onto both sides of a nickel foam strip 1 $cm \times 0.5\ cm$ yielding a total active area of 1 cm^2. The electrodes were then dried under vacuum at 80 ℃ for several hours. The loading of active material on the nickel foam was same for both materials as 2.0 mg cm^{-2}. After preparation of the working electrodes, CV, galvanostatic charge–discharge (GCD), and EIS measurements were performed using a three-electrode setup in 2 M KOH electrolyte within the frequency range of 10^{-2}-10^{5} Hz. Specific capacity (F g^{-1}), $C_{specific}$ values for both oxides were calculated by using the following Eq. (40), where Δt is discharge time, ΔV (volts) is voltage window, and $j = \frac{I}{m}$ is current density (A g^{-1}), current per unit active material mass.[107]

$$C_{specific} = \frac{j \times \Delta t}{\Delta V} \tag{40}$$

Figure 3.3 Conventional three-electrode set-up immersed in 2 M KOH.

3.4 Zinc-air Battery Performance Tests

The ZnAB was composed of a zinc plate serving as the anode, an air cathode made from either HRS or HSP, and an electrolyte solution of 6 M KOH containing 0.2 M zinc acetate, $Zn(CH_3COO)_2$, as an additive. The air cathode structure included a gas diffusion layer, electrocatalyst material, and a PTFE membrane. The performance of the battery was evaluated using a GAMRY Interface 1000 potentiostat/galvanostat/ZRA system and Neware Battery Tester/Analyzer. Charge–discharge polarization tests for ZnABs utilizing HRS and HSP were carried out over a current density range of 0 to 200 mA cm^{-2}. Prepared ZnAB cells fully discharged in 5 mA cm^{-2} current density to find out and compare battery capacities of electrocatalysts. The battery capacities were calculated by multiplying the current density applied to the ZnAB cell with the corresponding discharge time. The rate performance of electrocatalysts was evaluated through stepwise charge–discharge testing. Discharge steps were applied sequentially at current densities of 5, 10, 15, and 20 mA cm^{-2}. Following the discharge cycle, the ZnABs were charged in the same order of current densities: 5, 10, 15, and 20 mA cm^{-2}. The cycling stability of a ZnAB was assessed through repeated charge–discharge testing at a constant current density of 5 mA cm^{-2}, with each charge and discharge step lasting 5 minutes.

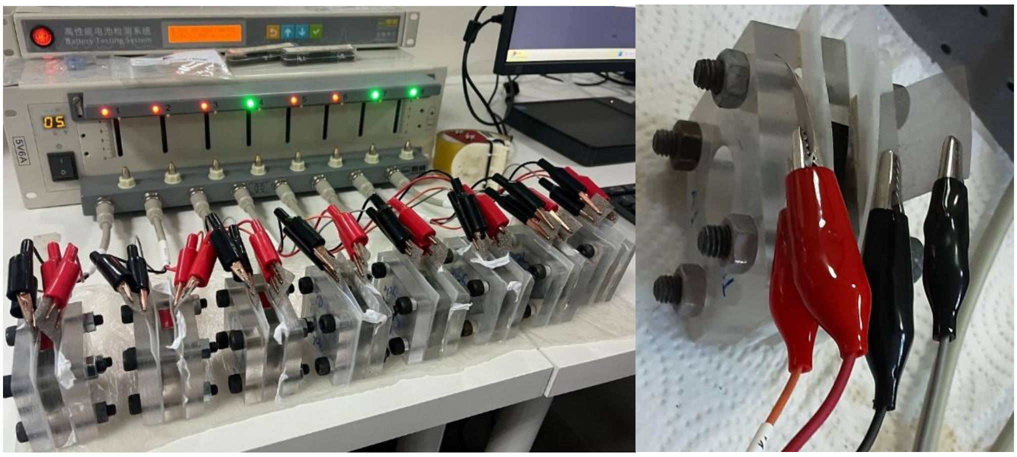

Figure 3.4 ZnAB cells used in laboratory.

3.5 Performance Evaluation of Supercapacitors

Device performance for supercapacitor applications was conducted using two-electrode setup in coin-cell (CR2032). The coin-cells were assembled as asymmetric supercapacitors with negative carbon electrodes, prepared by slurry of activated carbon with Super P carbon black and PVDF coated onto Ni Foil, placed opposite the working electrodes of HRS and HSP. Inks were prepared as described in the experimental section of capacitive electrode test. Prepared inks made from HRS and HSP were dropped onto Nickel foil for the positive electrode preparation. Another ink was made from activated carbon for the preparation of negative-carbon electrode similarly. Filter paper was used as a separator material swelled with 6 M KOH. After carefully sealing the negative electrode, spring, battery spacer, separator, positive electrode, and electrode cases using a crimping machine, the assembled cells were connected to the potentiostat via coin-cell clamps, as shown in Fig. 3.5. While evaluating the performance parameters of the asymmetric supercapacitors, the specific capacitance, $C_{specific}$ (F g^{-1}), energy density, $\hat{E}$, (Wh kg^{-1}), and power density (W kg^{-1}), $\hat{P}$, were determined using Eqs. (40-42).[108]

$$\hat{E} = \frac{C_{specific} \times \Delta V^2}{7.2} \tag{41}$$

$$\hat{P} = \frac{3600 \times \hat{E}}{\Delta t} \tag{42}$$

where ΔV represents discharge voltage window, and Δt is time passes during discharge.

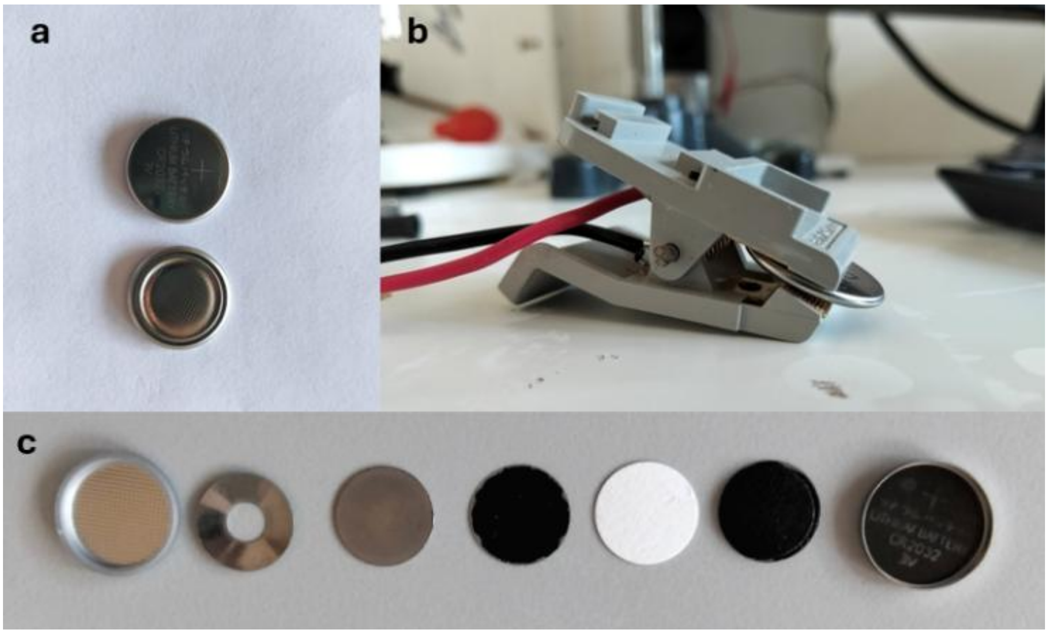

Figure 3.5 (a) Sealed coin cells (CR2032), (b) a coin cell clamp, and (c) internal components of a coin cell assembly.

CHAPTER 4

RESULTS AND DISCUSSION

Some parts of the results and discussions presented in this chapter have been previously published in a peer-reviewed journal article authored by the candidate. The data, figures, and analysis concerning the structural and electrocatalytic characterization of high-entropy oxides were originally reported in: Coskuner, A. B., Erdil, T., Ozgur, C., Geyikci, U., & Toparli, C. (2025). *Tuning the lattice strain through manipulating crystal structure of high entropy oxides enhances electrocatalytic performance*. *Materials Research Bulletin, 186*, 113333. https://doi.org/10.1016/j.materresbull.2025.113333.[109] The content has been adapted and extended where appropriate to align with the scope and format of the present thesis. All reuse of published material is done in accordance with the copyright policy of Elsevier, which permits authors to incorporate their own published work into their academic theses with appropriate citation.

4.1 Materials Structure

4.1.1 Crystal Structure

XRD experiments were done to learn about the crystal structure of the materials. The resulting XRD data, shown in Fig. 4.1a with corresponding planes, show that both HRS and HSP powders have a single cubic structure. There were no extra peaks that would mean there are other materials like different oxides or hydroxides. Rietveld fitting via GSAS-II was used to find out the unit cell parameters and the type of crystal structure. These results are shown in Fig. 4.1b for HRS and Fig. 4.1c for HSP. The crystal structure types (space groups) were $Fm\bar{3}m$ for HRS and $Fd\bar{3}m$ for HSP. The lattice parameters were 4.19 Å for HRS and 8.07 Å for HSP. The Rietveld refinement results are summarized in Table 4.1 for the HRS sample and in Table 4.2 for the HSP sample, as presented below.

Table 4.1 Refined structural parameters of HRS obtained from Rietveld analysis. Reproduced from Coşkuner et al., 2025, with permission from Elsevier.

<table>
<tr><td colspan="3">Material</td><td colspan="4">HRS, (NiCoCrCuAl)O</td></tr>
<tr><td colspan="3">Crystal Structure</td><td colspan="4">Rock-Salt</td></tr>
<tr><td colspan="3">Rw</td><td colspan="4">1.683%</td></tr>
<tr><td colspan="3">Space Group</td><td colspan="4">Fm-3m</td></tr>
<tr><td colspan="3">Cell Volume</td><td colspan="4">73.563 $Å^3$</td></tr>
<tr><td colspan="3">Crystal Density</td><td colspan="4">6.149 g cm^{-3}</td></tr>
<tr><td colspan="3">Lattice Parameter</td><td colspan="4">4.19 Å</td></tr>
<tr><td>Label</td><td>Wyckoff site</td><td>X</td><td>Y</td><td>Z</td><td>Atom</td><td>Occupation</td></tr>
<tr><td>Anion</td><td>4b</td><td>0.5</td><td>0</td><td>0</td><td>O</td><td>1</td></tr>
<tr><td>Octahedron</td><td>4a</td><td>0</td><td>0</td><td>0</td><td>Co</td><td>0.2</td></tr>
<tr><td>Octahedron</td><td>4a</td><td>0</td><td>0</td><td>0</td><td>Cr</td><td>0.2</td></tr>
<tr><td>Octahedron</td><td>4a</td><td>0</td><td>0</td><td>0</td><td>Cu</td><td>0.2</td></tr>
<tr><td>Octahedron</td><td>4a</td><td>0</td><td>0</td><td>0</td><td>Ni</td><td>0.2</td></tr>
<tr><td>Octahedron</td><td>4a</td><td>0</td><td>0</td><td>0</td><td>Al</td><td>0.2</td></tr>
</table>

Table 4.2 Refined structural parameters of HSP obtained from Rietveld analysis. Reproduced from Coşkuner et al., 2025, with permission from Elsevier.

Material				HSP, $(NiCoCrCuAl)_3O_4$		
Crystal Structure				Cubic Spinel		
Rw				4.554%		
Space Group				Fd-3m		
Cell Volume				526.358 $Å^3$		
Crystal Density				5.555 g cm^{-3}		
Lattice Parameter				8.07 Å		
Label	**Wyckoff site**	**X**	**Y**	**Z**	**Atom**	**Occupation**
Anion	32e	0.252	0.252	0.252	O	1
Octahedron	16c	0.5	0.5	0.5	Co	0.2
Octahedron	16c	0.5	0.5	0.5	Cr	0.2
Octahedron	16c	0.5	0.5	0.5	Cu	0.2
Octahedron	16c	0.5	0.5	0.5	Ni	0.2
Octahedron	16c	0.5	0.5	0.5	Al	0.2
Tetrahedron	8b	0.125	0.125	0.125	Co	0.2
Tetrahedron	8b	0.125	0.125	0.125	Cr	0.2
Tetrahedron	8b	0.125	0.125	0.125	Cu	0.2
Tetrahedron	8b	0.125	0.125	0.125	Ni	0.2
Tetrahedron	8b	0.125	0.125	0.125	Al	0.2

The broader diffraction peaks observed in the HRS sample compared to HSP can be linked to several possible causes. One contributing factor is the hydrogen-rich environment used during synthesis, which may influence peak broadening. Additionally, the finer particle and crystallite sizes associated with the HRS sample could play a role.[110] Another possible reason is the presence of considerable inhomogeneous microstrain in the structure[111], likely stemming from the significant ionic radius mismatch among the various elements. In contrast to HSP, the reducing conditions applied during HRS synthesis may lead to a partial reduction of metal ions, which can induce microstrain within the lattice. To further explore these structural differences, the Williamson–Hall (W-H) method[112] was applied. This technique analyzes peak profiles to estimate both crystallite size and microstrain in the high-entropy rock-salt (HRS) and spinel (HSP) oxides. As shown in Fig. 4.1d, the slope and intercept of the W-H plot correspond to the material's strain and crystallite size, respectively. While slightly higher intercept of HRS line indicates smaller crystallite size of it compared to HSP, additionally, the HRS sample shows a much steeper slope, implying a significantly higher degree of microstrain in its structure compared to HSP.

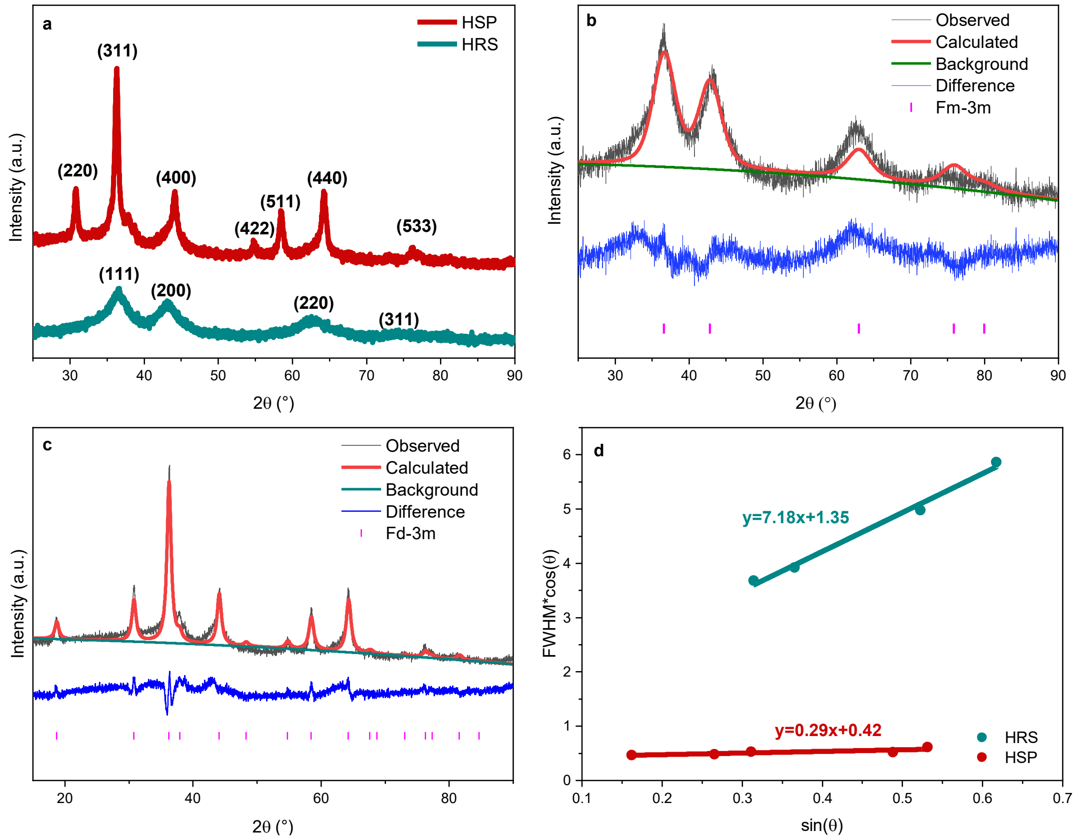

Figure 4.1 XRD patterns of (a) both HEO samples, (b) HRS with Rietveld Refinement, (c) HSP with Rietveld Refinement. (d) Williamson-Hall analysis of XRD data. Reproduced from Coşkuner et al., 2025, with permission from Elsevier.

Structural phase amounts were also simulated using Thermocalc for the corresponding compositions of HRS and HSP as a function of temperature, as shown in Fig. 4.2a and Fig. 4.2b, respectively. The simulation results revealed that both compositions (HRS and HSP) primarily contain spinel phases along with minor amounts of rock-salt (halite) phase. This result aligns well with the experimental observations, as the spinel phase in HSP has already been validated by XRD, and the HRS sample, treated under H_2 gas flow, possibly experienced a reduction of the spinel phase into the rock-salt (halite) phase. Consequently, the XRD results indicated the formation of the rock-salt (halite) phase.

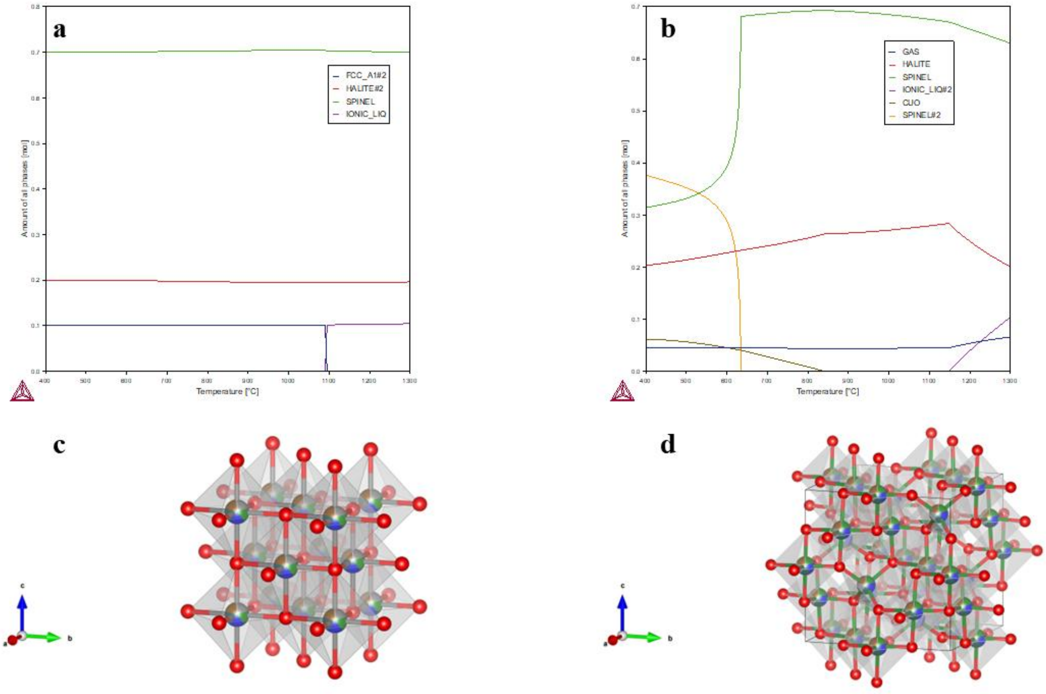

Figure 4.2 Thermocalc simulation results for (a) HRS and (b) HSP. VESTA illustrations of (c) HRS and (d) HSP.

Representative unit cells of HRS and HSP were constructed using VESTA software based on the XRD results and are illustrated in Fig. 4.2c and Fig. 4.2d, respectively. As a result of VESTA calculations, the metal–oxygen bond length was calculated as 2.094 Å for HRS in octahedral coordination. In the case of HSP, the bond lengths were found to be 1.891 Å and 1.942 Å for tetrahedral and octahedral coordination, respectively. This indicates that the metal–oxygen bonds in HSP are shorter than those in HRS. Based on the lattice structures visualized in Fig. 4.2c and Fig. 4.2d, the Madelung potentials for each type of site in both HRS and HSP structures were roughly calculated using VESTA and are reported in Table 4.3.

Table 4.3 Approximated Madelung potential values for each site in both crystal structures

HRS		HSP	
Wyckoff Site	**ϕ (eV)**	**Wyckoff Site**	**ϕ (eV)**
4a (octahedral)	~ -1.89	8a (tetrahedral)	~ -2.9
4b (Anion)	~ 1.60	16d (octahedral)	~ -1.95
		32e (Anion)	~ 1.71

4.1.2 Morphological and Surface Features of Particles

Scanning electron microscopy (SEM) and energy-dispersive X-ray spectroscopy (EDS) mapping were employed to examine the surface morphologies and elemental distributions of the HRS and HSP samples, as shown in Fig. 4.3a and Fig. 4.3b. The HRS sample is characterized by notably smaller and more compact particles, measuring approximately 0.6 to 0.9 μm in size. In contrast, the HSP sample consists of significantly larger particles (~20 μm) that exhibit a pronounced porous structure, with pore sizes ranging from 5 μm to 15 μm. Despite the larger particle size, the extensive porosity of HSP considerably enhances its overall surface area. Elemental mapping via EDS confirms a homogenous distribution of the primary elements, Ni, Co, Cu, Cr, Al, and O, throughout both HRS and HSP, with no signs of elemental segregation or clustering. Quantitative surface area measurements using the Brunauer–Emmett–Teller (BET) method reveal values of 147 $m^2\ g^{-1}$ for HRS and 112 $m^2\ g^{-1}$ for HSP.

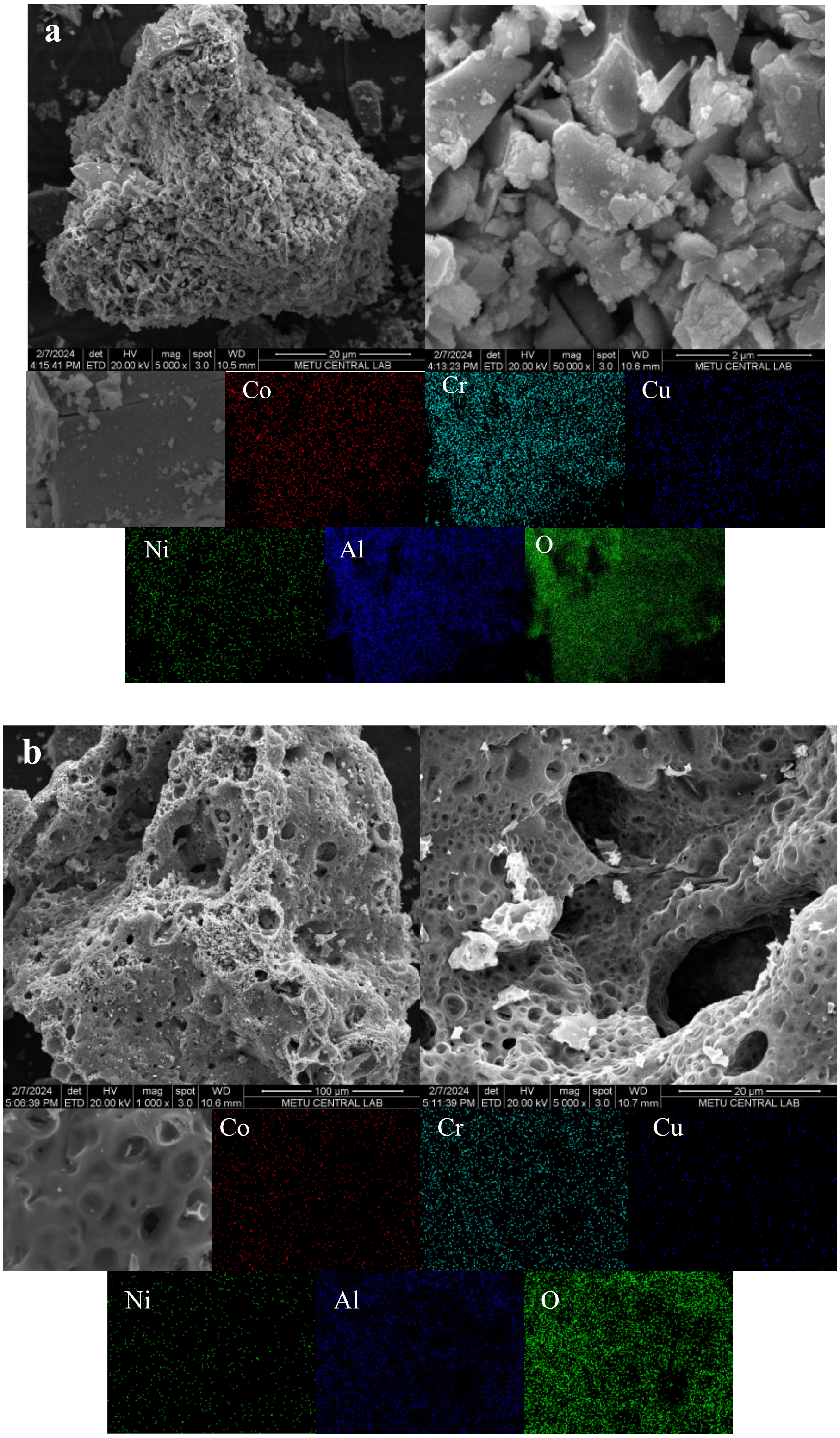

Figure 4.3 Surface and elemental distribution images for (a) HRS and (b) HSP. Reproduced from Coşkuner et al., 2025, with permission from Elsevier.

4.1.3 Electronic Structure

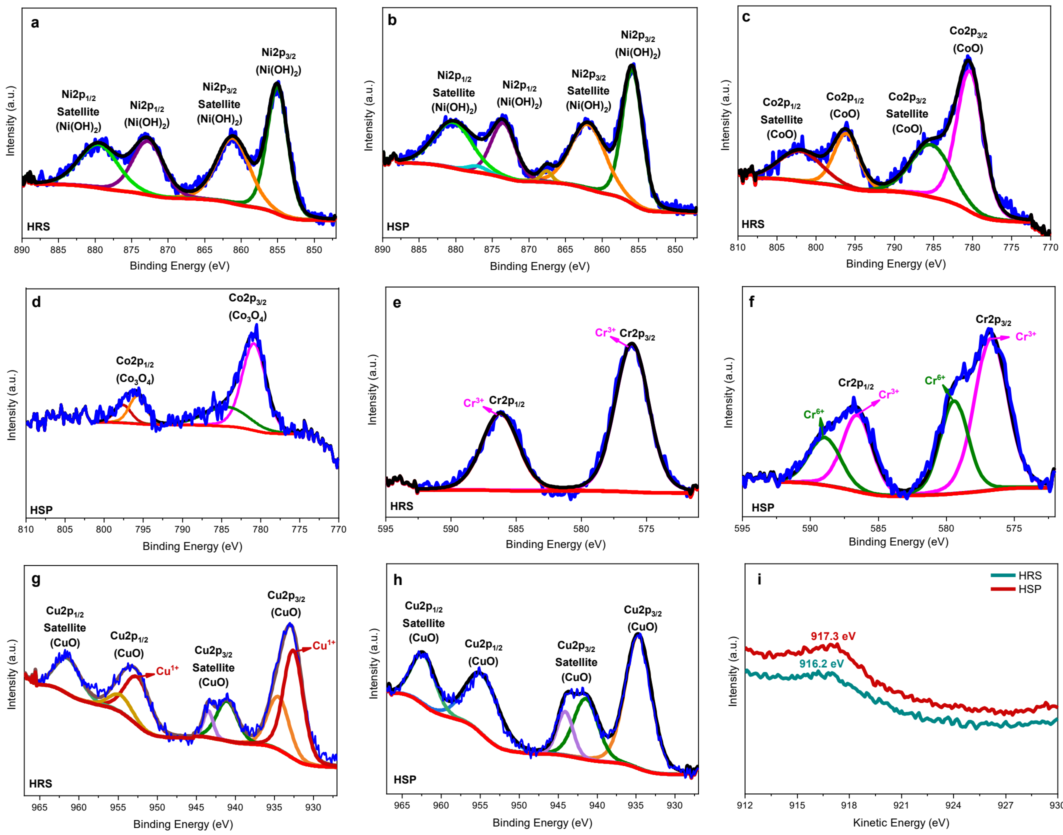

Figure 4.4 XPS core-level spectra of (a) Ni2p for HRS, (b) Ni2p for HSP, (c) Co2p for HRS, (d) Co2p for HSP, (e) Cr2p for HRS, (f) Cr2p for HSP, (g) Cu2p for HRS, (h) Cu2p for HSP, (i) Cu LMM for boh HRS and HSP. Modified from Coşkuner et al., 2025.

X-ray photoelectron spectroscopy, XPS, was utilized to determine the oxidation states of the elements in the structure. Fig. 4.4 presents the core-level spectra of Ni 2p, Co 2p, Cr 2p, and Cu 2p for both HRS and HSP samples. As shown in Fig. 4.4a and Fig. 4.4b, the presence of the Ni^{2+} oxidation state is confirmed by the characteristic Ni $2p_{3/2}$, Ni $2p_{3/2}$ satellite, Ni $2p_{1/2}$, and Ni $2p_{1/2}$ satellite peaks. These appear at 855.1, 861.2, 873.0, and 879.7 eV for HRS, and at 856.0, 862.1, 873.7, and 880.4 eV for HSP, respectively. As shown in Fig. 4.4c and Fig. 4.4d, the Co 2p spectrum of HRS exhibits four distinct peaks: Co $2p_{3/2}$, its satellite, Co $2p_{1/2}$, and its satellite, located at 780.5, 785.5, 796.3, and 802.1 eV, respectively. In contrast, the Co 2p spectrum of HSP displays only two primary peaks, Co $2p_{3/2}$ at 781.0 eV and

Co $2p_{1/2}$ at 796.1 eV, with no prominent satellite features. The absence of strong satellite peaks in HSP confirms the coexistence of Co^{2+} and Co^{3+} oxidation states, as typically observed in spinel structures.[113] Conversely, the presence of only Co^{2+} peaks in HRS is consistent with the characteristics of rock-salt structures. The XPS spectrum of chromium, shown in Fig. 4.4e shows that the HRS sample only exhibits Cr^{3+} peaks at 576.2 eV and 586.0 eV. In contrast, Fig. 4.4f reveals both Cr^{3+} and Cr^{6+} states in the HSP sample where Cr^{3+} peaks appear at 576.7 eV for Cr $2p_{3/2}$ and 586.6 eV for Cr $2p_{1/2}$, while Cr^{6+} peaks are found at 579.4 eV and 589.0 eV, respectively. The presence of both Cr^{3+} and Cr^{6+} has also been reported in other spinel oxides, such as $NiCr_2O_4$, where similar peak fitting methods were used.[114] This difference between HRS and HSP is expected, since HRS was treated in a hydrogen atmosphere, which leads to the reduction of metal cations, including chromium. The XPS spectra of copper, shown in Fig. 4.4g and Fig. 4.4h, look very similar for both HRS and HSP, which suggests the presence of Cu^{2+} in both structures. However, in the case of HRS, some Cu^{+} ions may also be present. A similar observation was made in a study[115], where the Cu 2p spectrum of a rock-salt structured high entropy oxide included both Cu^{+} and Cu^{2+}. In our analysis of the Cu $2p_{3/2}$ and Cu $2p_{1/2}$ peaks in Fig. 4.4g, we also added Cu^{+} peaks to properly fit the spectrum for HRS. To further verify the presence of Cu^{+} species in the HRS sample, Cu LMM Auger spectra were collected and are shown in Fig. 4.4i. Based on previous studies[116,117], the Cu LMM Auger peaks associated with Cu^{+} (as in Cu_2O) and Cu^{2+} (as in CuO) typically appear at kinetic energies of approximately 916.8 eV and 917.6 eV, respectively. In the present study, the Cu LMM peak for HRS is observed at a slightly lower kinetic energy (~916.2 eV) than that of HSP (~917.3 eV), which supports the inference that Cu^{+} is the dominant oxidation state in the HRS structure. For the Cu^{2+} state (similar to CuO), the Cu $2p_{3/2}$, Cu $2p_{3/2}$ satellite, Cu $2p_{1/2}$, and Cu $2p_{1/2}$ satellite peaks for HRS appear at 933.0, 941.2, 943.3, 953.4, and 961.7 eV, respectively. The same peaks for HSP were found at binding energies: 934.8, 941.8, 943.6, 955.3, and 962.5 eV. As seen in the Ni 2p, Cr 2p, and Cu 2p spectra, binding energies were measured slightly higher in HSP. This is possibly the result of existing higher valance states within the structure.[118] Madelung potentials are expected to be higher when structure having higher valance states (ion charges) of the cations and shorter bond-distances (ion-separations).[119]

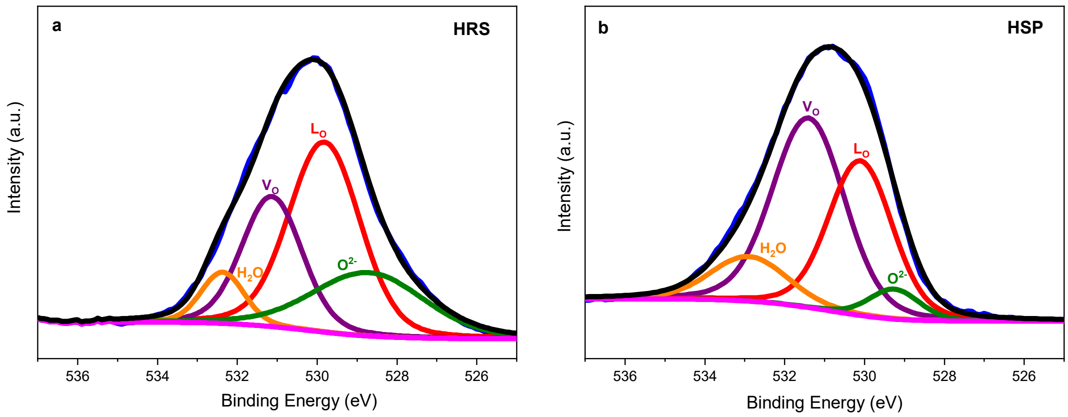

Figure 4.5 Core-level XPS spectra of O1s for (a) HRS and (b) HSP, respectively Modified from Coşkuner et al., 2025.

The O 1s XPS spectra of the synthesized materials are presented in Fig. 4.5a and Fig. 4.5b. The main O 1s peak is centered at 530.1 eV for HRS and at 530.9 eV for HSP. As studies reveal, a higher Madelung potential at oxygen sites indicates stronger electron binding; in other words, a lower Madelung potential facilitates electron removal from oxygen.[120,121] Since the Madelung potential at the oxygen sites was calculated to be higher for HSP, as shown in Table 4.3, theoretically, O 1s spectrum of HSP is expected to shift toward higher binding energies compared to HRS, as observed experimentally in Fig. 4.5a and Fig. 4.5b. Another reason for observing lower binding energy in the overall O1s spectra of HRS can be attributed to its higher ionic character, as it was stated in a previous study[122] that a shift towards lower binding energies is observed in O1s spectra when the ionic character of species increases. Oxides can be categorized according to their degree of ionic or covalent bonding based on the position of their O 1s peaks. Those exhibiting peaks between 530.5 and 533 eV are considered semi-covalent oxides (SCO), while those with O 1s peaks in the 529.6–530.4 eV range fall under the classification of normal ionic oxides (NIO).[123] Based on this approach, the O 1s peak positions suggest that HRS aligns with the characteristics of NIOs, whereas HSP shows features consistent with SCOs. Nevertheless, the emphasis here is not on rigidly assigning these labels, but rather on comparing the relative ionic character of the two samples using their O 1s spectra. The more pronounced ionic character of HRS can be attributed to its fully octahedral coordination environment, where coordination number is 6, for both cations and anions, in contrast to HSP, which exhibits a combination of octahedral and tetrahedral sites, leading to a coordination number range of 4 to 6. As seen in Fig. 4.5a, two peaks are observed at 529.9 eV and 531.2 eV, corresponding to lattice oxygen (L_O) and oxygen vacancies (V_O), respectively in the HRS structure. For HSP, these peaks appear at slightly higher binding energies of 530.1 eV and 531.4 eV as shown in Fig. 4.5b. The peak related to oxygen vacancies covers 26% of the total O 1s area in HRS, while this proportion increases to 48 % in HSP. This suggests that the HSP structure contains a higher amount of oxygen vacancies compared to HRS. Even though XPS analysis indicates a higher concentration of oxygen vacancies in HSP compared to HRS, XRD findings suggest that HSP shows lower levels of inhomogeneous strain. A previous study reported that oxygen vacancies can contribute to lattice distortion.[101] Taken together, these findings suggest that the observed microstrain originates primarily from the crystal structure rather than the presence of oxygen vacancies. In other words, although HRS contains fewer oxygen vacancies, it exhibits greater microstrain.

4.2 OER, ORR, and Zn-air Battery Performance of Spinel and Rock-Salt Structured HEOs

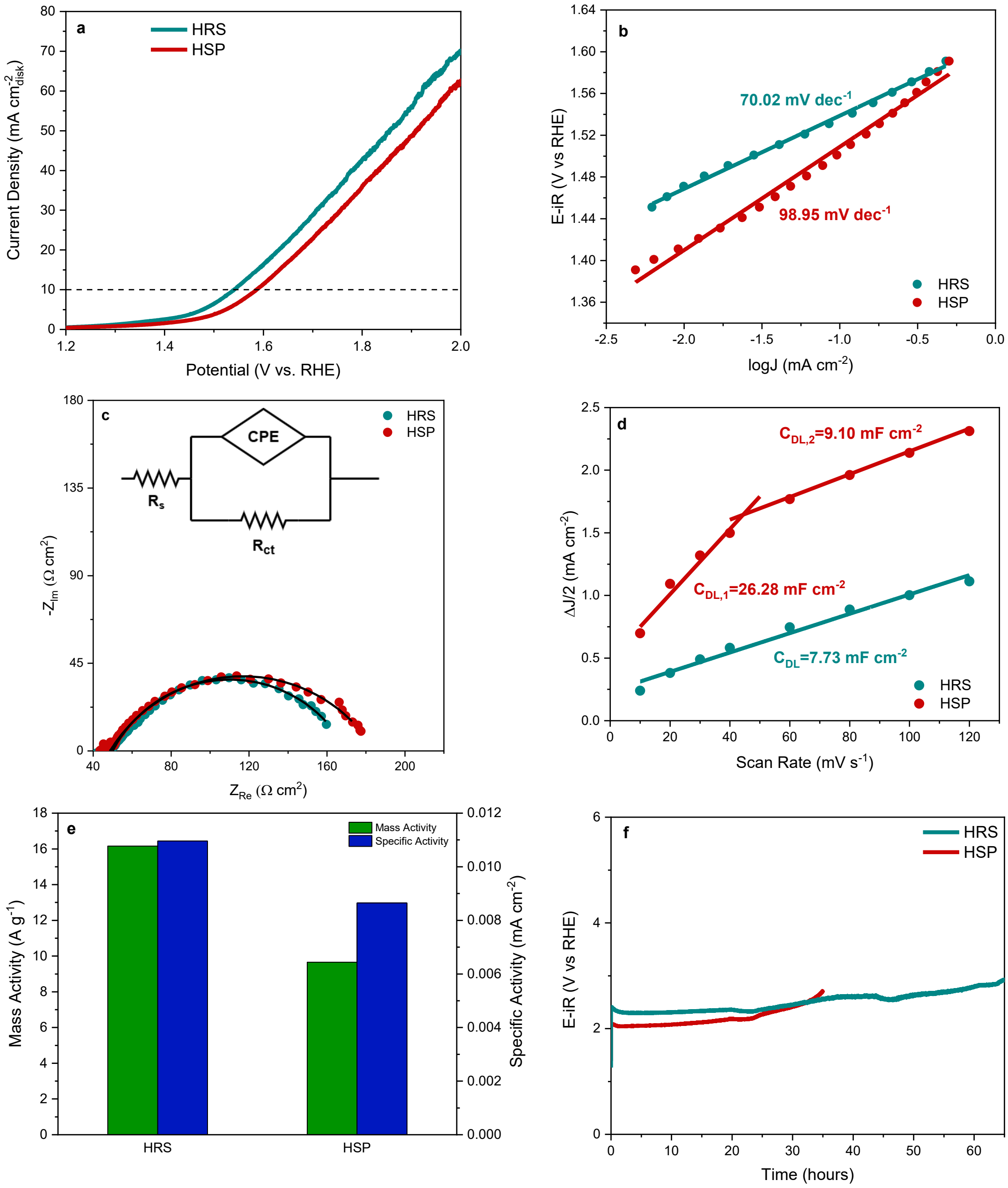

Figure 4.6 (a) LSV results of OER, (b) tafel plots of OER, (c) resulting Nyquist curves from EIS, (d) electrical double-layer capacitance plots, (e) activity comparison, and (f) galvanostatic durability curves for HRS and HSP. Reproduced from Coşkuner et al., 2025, with permission from Elsevier.

Electrochemical performance of HRS and HSP was evaluated using a standard three-electrode setup in an oxygen-saturated 0.1 M KOH electrolyte. The system included a rotating glassy carbon disk as the working electrode, a platinum wire as the counter electrode, and an Ag/AgCl electrode serving as the reference. Linear sweep voltammetry (LSV) measurements were performed with internal resistance (IR) compensation and normalized based on the geometric surface area of the glassy carbon electrode, which was 0.07068 cm^2.

In the oxygen evolution reaction (OER), HRS demonstrates an overpotential of 311 mV at a current density of 10 mA cm^{-2}, which is lower than the 357 mV observed for HSP. According to previous reports, IrO_2, a widely used benchmark OER electrocatalyst, exhibits an overpotential of approximately 400 mV in a 1 M KOH solution.[124] Notably, both HRS and HSP achieve lower overpotentials than IrO_2, even though the measurements were conducted in a more dilute electrolyte (0.1 M KOH).

Beyond overpotential evaluation, Tafel slope analysis was conducted using chronoamperometric measurements to assess and compare the OER kinetics of the materials. Stepwise chronoamperometry, as seen in Fig. 4.7a, was employed to ensure that a steady-state current was achieved at each applied potential during the OER process. The Tafel slopes were determined to be 70.02 mV dec^{-1} for HRS and 98.95 mV dec^{-1} for HSP. As shown in Fig.4.6a–b, both the LSV curves and Tafel slope values indicate that HRS possesses enhanced catalytic performance toward the OER in comparison to HSP. This improved activity may be associated with the greater microstrain present in the HRS structure relative to that of HSP.

Electrochemical impedance spectroscopy (EIS) was performed to evaluate the charge-transfer behavior of the electrocatalysts, as shown in Fig. 4.6c. The experimental data were fitted using an equivalent circuit model[125] comprising solution resistance (Rs), charge-transfer resistance (Rct), and a constant phase element (CPE). Based on this fitting, the Rct values were determined to be approximately 120 Ω for HRS and 136 Ω for HSP. These findings indicate that HRS exhibits lower charge-transfer resistance compared to HSP, implying improved electrical conductivity. The exponents of the CPE, a, were determined to be 0.70 and 0.65 for HRS and HSP, respectively, indicating that the surfaces of both materials deviate similarly from ideal capacitive behavior under the given experimental conditions. The capacitance values derived from the constant phase element (CPE) were calculated as 1.924 and 6.931 mS s^a cm^{-2} for HRS and HSP, respectively, in 0.1 M KOH electrolyte. Consequently, the double-layer capacitance of HSP is approximately 3.60 times that of HRS based on the EIS analysis.

The double-layer capacitance, C_{DL}, which serves as an indicator of the electrochemically active surface area of the catalysts, was determined from cyclic voltammetry (CV) measurements conducted at scan rates of 10, 20, 30, 40, 60, 80, 100, and 120 mV s^{-1}, within the potential window of 0.20–0.30 V in 1 M KOH as represented in Fig. 4.7b-c. Based on these measurements, the calculated C_{DL} value was 7.73 mF cm^{-2} for HRS. For the HSP sample, two distinct double-layer capacitance values were obtained: one at lower scan rates, denoted as $C_{DL,1}$, and the other at higher scan rates, denoted as $C_{DL,2}$. As shown in Fig. 4.6d, $C_{DL,1}$ was calculated to be 26.28 mF cm^{-2}, and while $C_{DL,2}$ was found to be 9.10 mF cm^{-2}. Due to the highly porous nature and large pore sizes of HSP, the lower C_{DL} value observed at higher scan rates can be attributed to limited ion accessibility to the inner active surface regions within the short time frame. Consequently, the evaluation of double-layer capacitance at high scan rates may not accurately reflect the full electrochemically active surface area; in other words, using high scan rates may lead to underestimation of C_{DL} in highly porous materials.[126] Therefore, $C_{DL,1}$ is considered a more representative value for the double-layer capacitance of HSP. These findings indicate that the double-layer capacitance of HSP is approximately 3.40 times that of HRS in 1 M KOH, supporting the capacitance ratio of 3.60 derived from EIS measurements.

To assess the intrinsic OER performance, both mass and specific activities were evaluated. Mass activity was calculated using the mass of the catalyst, while specific activity was determined relative to the BET surface area. The HRS sample exhibited a mass activity of 16.16 A g^{-1} and a specific activity of 0.01096 mA cm^{-2}, whereas HSP demonstrated values of 9.66 A g^{-1} and 0.00865 mA cm^{-2}, respectively, as presented in Fig. 4.6e. Long-term durability was examined by galvanostatic measurements at a constant current density of 10 mA cm^{-2}. As shown in Fig. 4.6f, HRS maintained its stability for approximately 75 hours, significantly longer than HSP, which remained stable for about 35 hours.

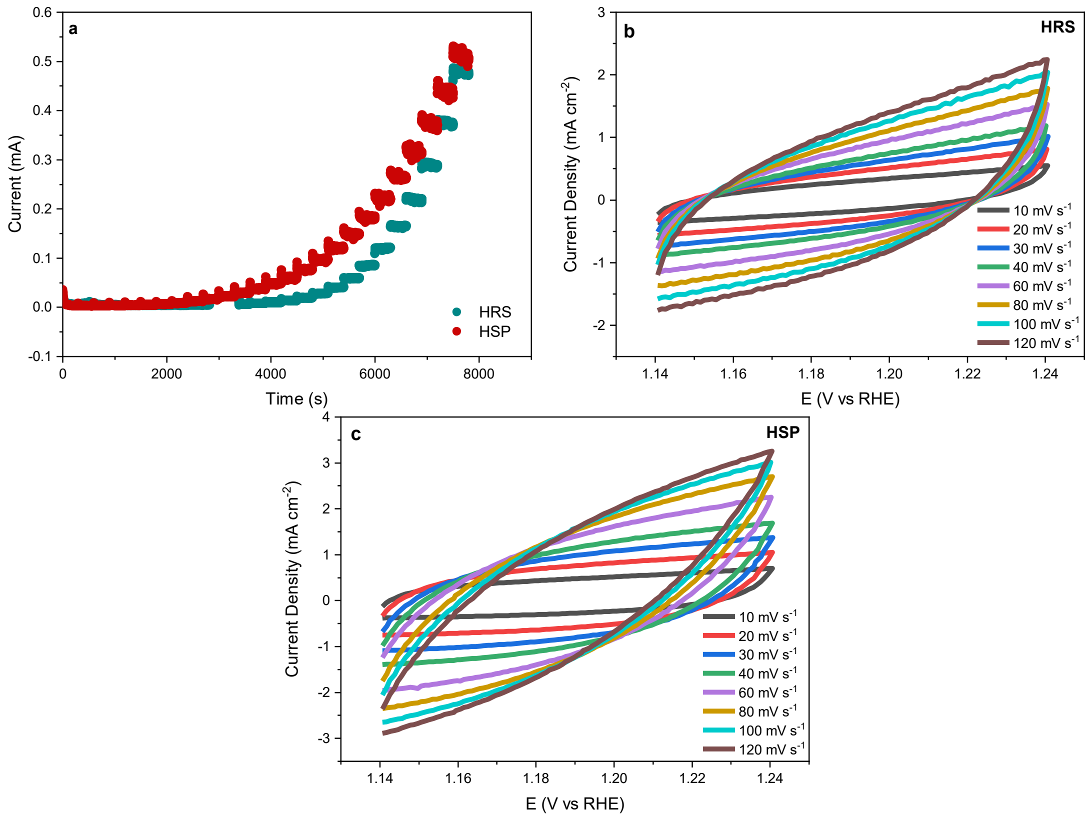

Figure 4.7 (a) Chronoamperometry measurements for Tafel analysis. CV curves for ECSA measurements of (b) HRS and (c) HSP. Reproduced from Coşkuner et al., 2025, with permission from Elsevier.

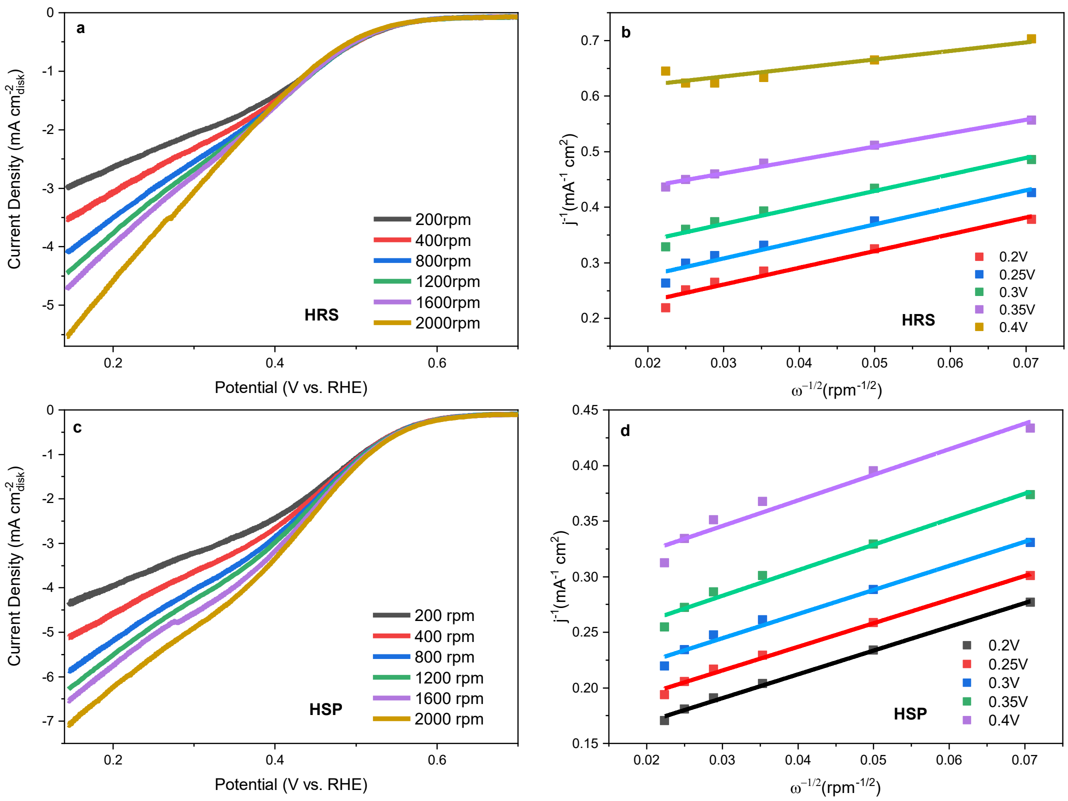

Figure 4.8 KL analysis**:** (a) LSV measurements of HRS recorded at varying electrode rotation rates, (b) corresponding linearized KL plots for HRS, (c) LSV curves of HSP at different rotation speeds, and (d) linearized KL plots derived from HSP data. Reproduced from Coşkuner et al., 2025, with permission from Elsevier.

In contrast, HSP demonstrates superior electrocatalytic performance toward the oxygen reduction reaction (ORR) compared to HRS, as shown in Fig. 4.9a. For reference, the commercial Pt/C catalyst typically delivers a current density of approximately 5 mA cm^{-2} at 0.20 V vs. RHE in 0.1 M KOH.[124] While this performance surpasses that of HRS, it remains lower than the ORR activity exhibited by HSP. Based on the O 1s XPS spectra, HSP contains a higher concentration of oxygen vacancies compared to HRS. This could contribute to its enhanced ORR activity, as supported by the experimental findings. The Tafel slope values for ORR were determined to be 226 mV dec^{-1} for HRS and 132 mV dec^{-1} for HSP, as illustrated in Fig. 4.9b.

A separate set of LSV measurements was carried out to estimate the number of electrons involved in the ORR pathway. The LSV profiles were recorded at various electrode rotation rates, 200, 400, 800, 1200, 1600, and 2000 rpm, as shown in Fig. 4.8. These data were then analyzed using the Koutecky-Levich (KL) approach by plotting the inverse current density against the inverse square root of the rotation speed.

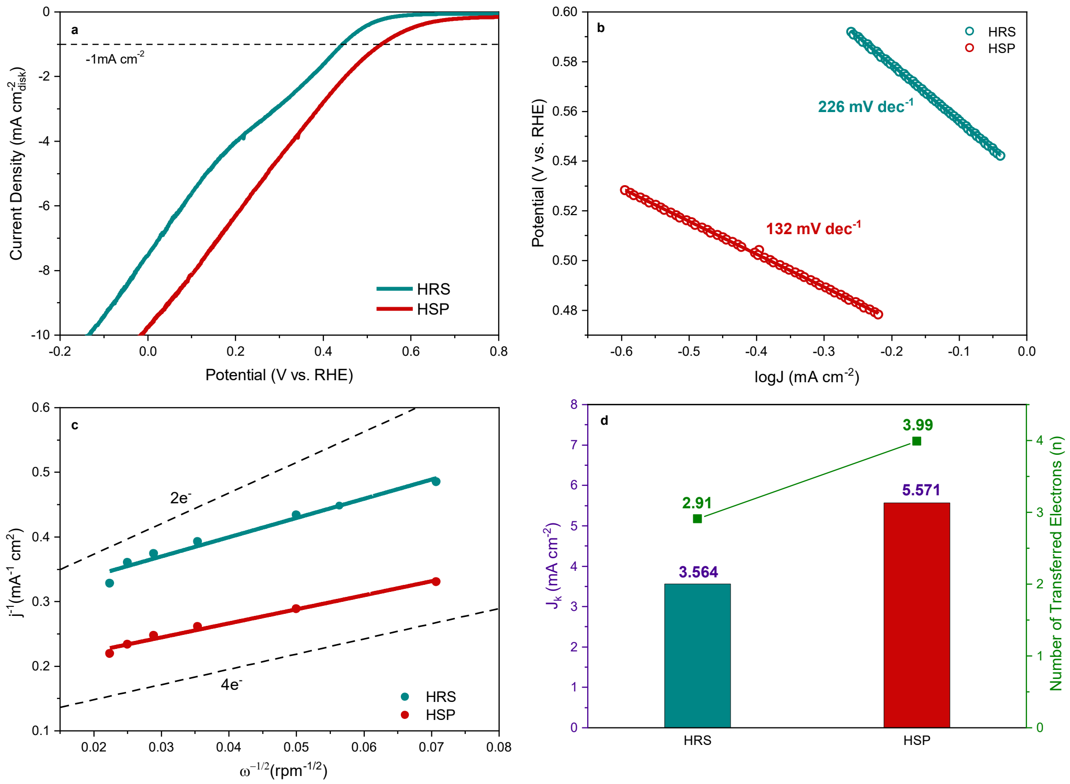

Figure 4.9 (a) LSV curves for ORR, (b) corresponding Tafel slopes, (c) linearized KL plots, and (d) summary of KL analysis results for both HRS and HSP. Reproduced from Coşkuner et al., 2025, with permission from Elsevier.

The resulting KL plots are presented in Fig. 4.9c. Based on the slopes of these plots, the electron transfer numbers were determined to be 2.91 for HRS and 3.99 for HSP. According to the KL-analysis, the kinetic current densities for ORR were calculated to be 3.564 mA cm^{-2} for HRS and 5.571 mA cm^{-2} for HSP, as illustrated in Fig. 4.9d. The oxygen reduction reaction (ORR) can proceed via two distinct pathways: a four-electron route that reduces O_2 directly to hydroxide ions (OH^-), and a two-electron route in which O_2 is partially reduced to form peroxide ions, $(HO_2)^-$.[127] The KL-analysis indicates that on the HRS surface, both the two-electron and four-electron ORR pathways are active, as the calculated electron transfer number is closer to two. This suggests that molecular oxygen is partially reduced to peroxide ions, $(HO_2)^-$. In contrast, the electron transfer number for HSP is nearly four, implying that the ORR proceeds predominantly via the four-electron route, resulting in the complete reduction of O_2 to hydroxide ions (OH^-). These findings are consistent with the initial LSV results shown in Fig. 4.9a, further confirming the superior ORR activity of HSP. This enhanced performance can be attributed to its ability to favor the four-electron pathway and its higher kinetic current density.

The bifunctional performance of the electrocatalysts was assessed using the bifunctional index (BI), defined as the potential difference between the OER at a current density of 10 mA cm^{-2} and the ORR at –1 mA cm^{-2}. A lower BI value corresponds to better overall bifunctional activity. The BI values were calculated as 1.09 V for HRS and 1.05 V for HSP, suggesting that HSP possesses a slightly superior bifunctional electrocatalytic capability. While a lower BI value reflects enhanced catalytic efficiency for both OER and ORR, it primarily derives from short-term LSV measurements and does not fully capture the long-term performance required for practical zinc–air battery (ZnAB) applications. In such systems, the durability of the electrocatalyst—particularly its ability to retain structural integrity over extended operation—is crucial. Although the BI values of HRS and HSP differ only slightly, a substantial gap exists in their long-term stability, as demonstrated in Fig. 4.6f. This notable contrast highlights HRS as a more promising candidate for real-world applications, where both fast reaction kinetics and structural robustness are essential.

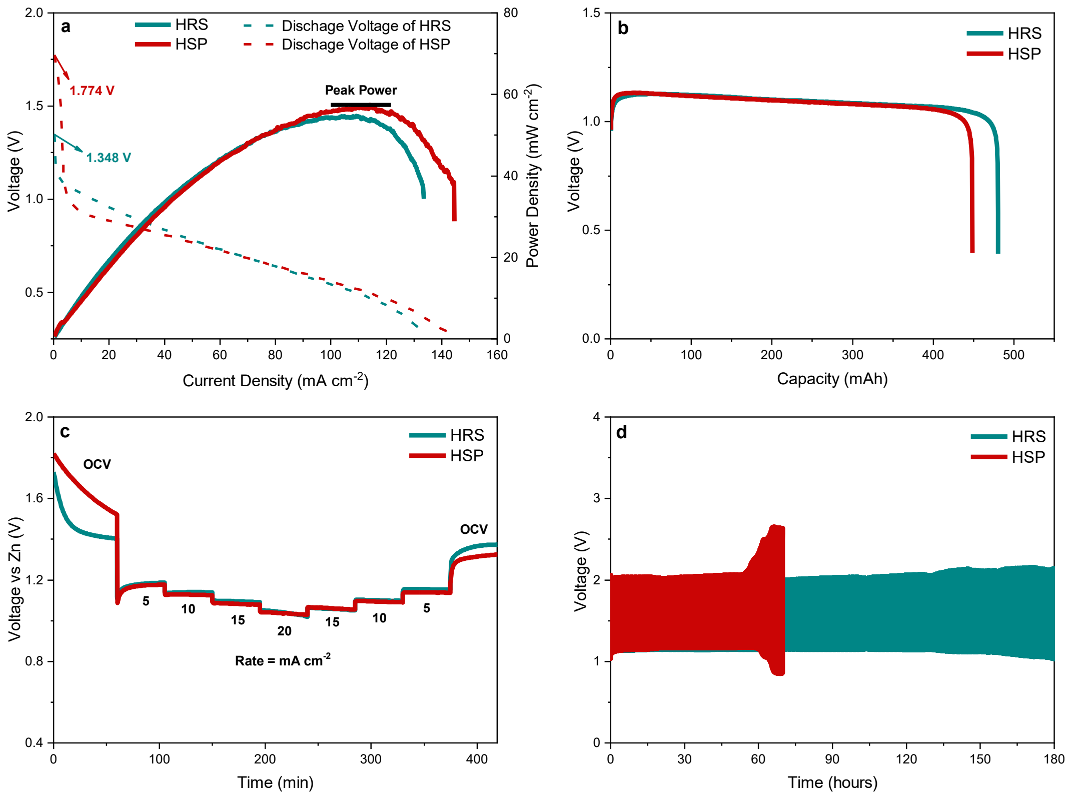

Figure 4.10 (a) Power–voltage polarization profiles, (b) discharge curves under full discharge conditions, (c) multistep charge–discharge behavior, and (d) cyclic charge–discharge performance at a current density of 5 mA cm^{-2} for HRS and HSP. Reproduced from Coşkuner et al., 2025, with permission from Elsevier.

In the case of ZnAB performance evaluations, the open-circuit potential of the Zn–air battery employing the HSP cathode was recorded as 1.82 V, which is higher than that of the HRS-based cell, measured at 1.73 V. Fig. 4.10a presents the charge–discharge polarization curves for both electrocatalysts. The results show that HSP delivers a higher discharge voltage of 1.77 V, compared to 1.35 V for HRS. The peak power densities were determined to be 54.6 mW cm^{-2} at 108 mA cm^{-2} for HRS and 56.9 mW cm^{-2} at 114 mA cm^{-2} for HSP. Considering both discharge voltage and peak power density, the ZnAB incorporating the HSP cathode demonstrates superior power output compared to its HRS-based counterpart. This observation aligns with the ORR performance of the electrocatalysts, as the oxygen reduction reaction governs the discharge process in Zn-air batteries.

The discharge capacity profiles of Zn–air batteries utilizing HRS and HSP cathodes at a current density of 5 mA cm^{-2} are presented in Fig. 4.10b. The battery assembled with the HRS cathode delivers a higher capacity of approximately 480 mAh, compared to around 450 mAh for the HSP-based cell. The Zn–air batteries incorporating HRS and HSP cathodes demonstrate similar rate performance and operational stability. As Fig. 4.10c revealed, the output voltage of the HRS-based cell remained at 1.37 V, corresponding to 79.4% of its initial value (1.73 V), after 400 minutes of testing. In comparison, the HSP-based battery retained a final voltage of 1.33 V, which is 72.8% of its initial output (1.82 V). These results indicate that the HRS cathode provides superior stability and rate capability under prolonged operation.

As illustrated in Fig. 4.10d, the ZnAB employing the HRS cathode operated for an extended duration of approximately 180 hours within a stable potential window of 0.87 V, showing no signs of degradation. In contrast, the HSP-based cell sustained operation for only around 60 hours under the similar voltage window. As can be seen from Fig. 4.10d, it obviously started to degrade at the 70th hour by widening the voltage window. This notable difference in stability may be attributed to the lattice distortion arising from the large atomic-size mismatch of the components likely to be larger in the HRS structure. Given that both electrocatalysts are composed of identical metal cations in equimolar proportions (1/5 each), their configurational entropy might be assumed similar, 1.6094R. However, beyond configurational entropy, contributions to the stability of the material those arising from microstrain, must also be considered, as noted.[93] Since XRD analysis indicates a possibility of higher degree of microstrain in HRS, it might be reasonable to conclude that its larger microstrain in addition to configurational entropy likely contributes to the improved phase stability observed in HRS, reinforcing its suitability as a chemically stable, single-phase electrocatalyst.

4.3 Exploring Supercapacitor and Capacitive Characteristics

To investigate the electrochemical behavior of the synthesized high-entropy oxides as electroactive materials for supercapacitor applications, three-electrode experiments were conducted in a 2 M KOH electrolyte. The first step of the electrochemical characterization involved cyclic voltammetry (CV) measurements at various scan rates ranging from 1 to 50 mV s^{-1}. Since these materials were evaluated for supercapacitor use, the CV voltage window was set between 0.0 - 0.50 V for HRS and 0.0 - 0.55 for HSP to prevent water splitting reactions at the working and counter electrodes. Voltage window was selected 50 mV higher for HSP because as observed from the OER experiments, overpotential of HSP is approximately 50 mV higher than that of HRS for various current densities.

Although the CV curves of HRS do not exhibit sharp redox peaks shown in Fig. 4.11a, on the other hand, as seen in Fig. 4.11b, sharper redox peak can be observed, particularly in the HSP sample. The reason for observing relatively smoother curves in the CV curves might be related to existence of multiple metals with different redox potentials.[128]

Based on the cathodic peaks occurred in the both CV data, the charge storage mechanisms of the high-entropy oxides were examined. As discussed earlier in the literature review, see Eq. (19), b-value analysis was performed. By taking the logarithm of both sides of Eq. (19), the data were linearized and fitted to straight lines, as shown in Fig. 4.11c. The slopes of these lines represent the b-values for each active material and calculated as 0.76 and 0.51 for HRS and HSP, respectively. As stated in the literature review chapter, the b-value close to 1, in between 0.5 and 1.0, indicates that surface-controlled processes dominate over diffusion, suggesting that the charge storage mechanism in HRS is primarily surface-driven. On the other hand, the b-value close to 0.5 indicates purely battery-type behavior, where the charge storage mechanism in HSP is governed by diffusion-controlled processes.

When it comes to analyzing CV data for supercapacitor materials, the method developed by Dunn and co-workers yields quite accurate results.[129] To understand the capacitive and diffusion-controlled (battery-type) characteristics of the materials, Eq. (43) is used, where k_1 represents the capacitive contribution and k_2 represents the diffusion contribution.[130]

$$i(V) = k_1 v + k_2 v^{1/2} \tag{43}$$

According to Fig. 4.11d, HRS again shows a predominantly capacitive contribution, with more than 90%. In contrast, Fig. 4.11e indicates that HSP exhibits a mainly diffusion-controlled contribution, exceeding 70%, as expected. Both the b-value (power law) analysis and Dunn's method confirm that the charge storage mechanism is predominantly surface-controlled (capacitive-type) for HRS, and mainly diffusion-controlled (battery-type) for HSP. If the particle size of an oxide powder decreases, the charge storage mechanism becomes more surface-controlled and less diffusion-controlled, as supported by experimental evidence in a previous study.[129] As shown in the SEM images in Fig. 4.3a and Fig. 4.3b, HRS exhibits significantly smaller particle sizes compared to HSP. Therefore, it might be expected to exhibit a higher capacitive contribution and a lower diffusion contribution than HSP.

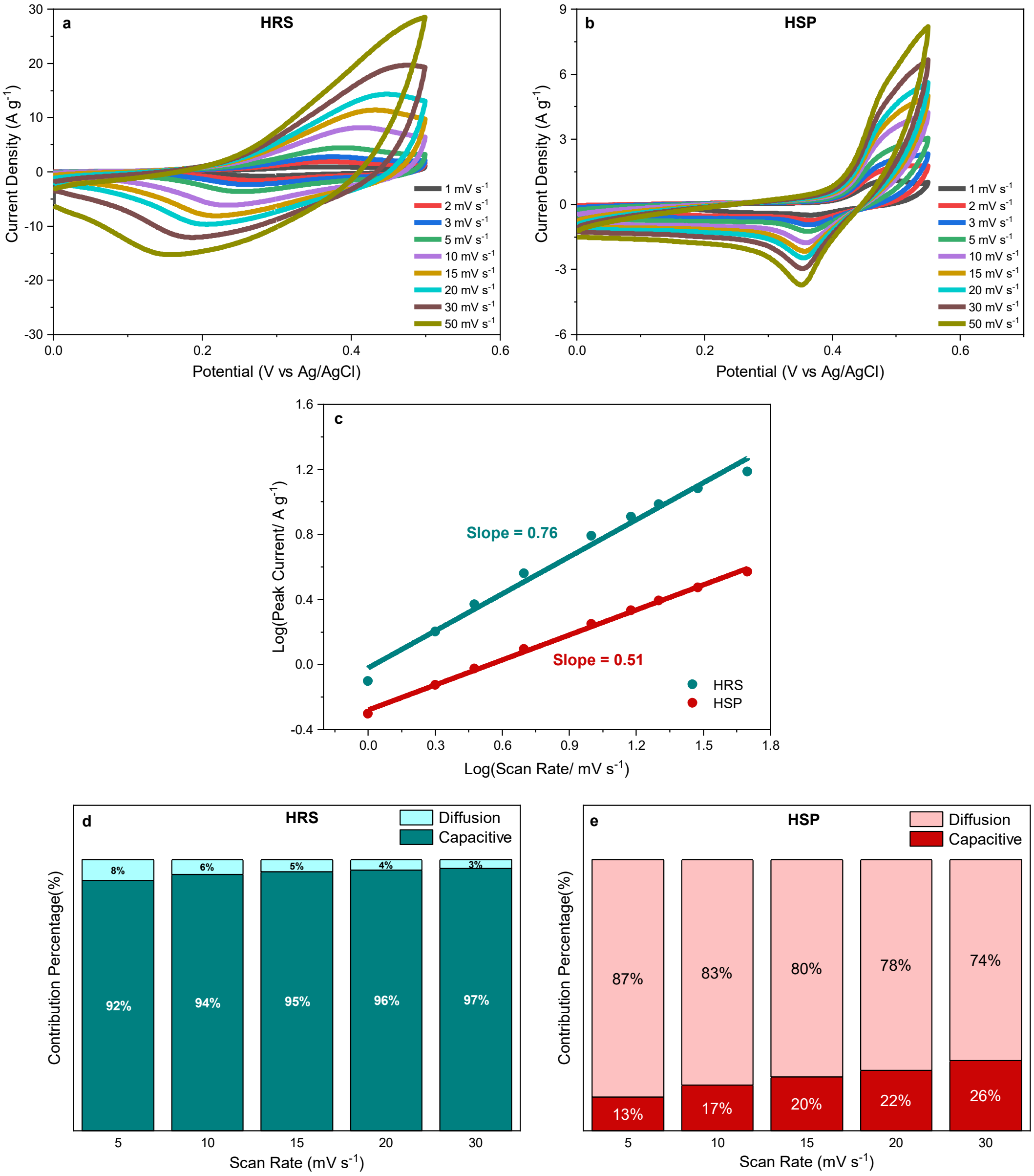

Figure 4.11 Three electrode cyclic voltammetry results for (a) HRS and (b) HSP, (c) power-law (b-value) plot, capacity contributions for (d) HRS and (e) HSP.

The pseudocapacitive performance of the materials was examined in three electrode set-up through GCD experiments at various current densities, along with cyclic durability tests. In addition to performance evaluation, the GCD plots also qualitatively reveal the charge storage behavior based on their shape. As explained in the literature review chapter, the presence of a plateau-like region in the GCD curve at a constant voltage indicates a battery-like charge storage process. Compared to HRS in Fig. 4.12a, HSP exhibits a more pronounced plateau-like behavior in Fig. 4.12b. The specific capacitances (F g^{-1}) were calculated using Eq. (40), based on the discharge time (s), voltage window (V), and various current densities (A g^{-1}) from the GCD plots, as shown in Fig. 4.12a and Fig. 4.12b for HRS and HSP, respectively. For HRS, specific capacitance values were calculated as 307, 302, 300, 292, and 267 F g^{-1} at current densities of 0.5, 1.0, 1.5, 2.0, and 5.0 A g^{-1}, respectively. In the case of HSP, the corresponding values were 166, 152, 132, 110, and 43 F g^{-1} at the same current densities. The cyclic durability of the materials in a three-electrode setup was investigated through cyclic charge–discharge experiments at a current density of 2 A g^{-1}, as shown in Fig. 4.12c. Both materials exhibited approximately 95% capacity retention after 1000 cycles.

EIS experiments were performed using the same three-electrode setup, and the resulting graphs are presented in Fig. 4.12d as dotted plots. These graphs were fitted according to the circuit model proposed in a previous study[131,132] for metal oxide-based pseudocapacitor materials. CPE2 is added to the circuit as shown on Fig. 4.12d to represent the non-ideal capacitive behavior resulting from potential-dependent Faradaic reactions.[131] The fitted curves and the corresponding equivalent circuit diagram are also shown in Fig. 4.12d. From the curve fitting of the EIS results, the equivalent series resistance (Rs) was determined to be 1.055 Ω for HRS and 0.740 Ω for HSP. Since pseudocapacitor materials are also evaluated in terms of their surface redox activity, the charge-transfer resistance (Rct) serves as a key indicator of redox performance.[133] The Rct values for HRS and HSP were calculated as 5.5 Ω and 14.0 Ω, respectively. As expected, HRS exhibits lower charge-transfer resistance, consistent with its surface-dominated charging behavior involving surface redox reactions. Another EIS result supports the diffusion-controlled charging nature of HSP. The Warburg impedances (Zw) were calculated as 0.155 and 0.078 S√s for HRS and HSP, respectively. Zw corresponds to the resistance to mass transport[133]; in other words, ionic species in the electrolyte encounter less resistance when diffusing into electrode-electrolyte interface of HSP. This result may also support the presence of the diffusion in HSP. To assess the ideality of capacitive behavior, the constant phase element (CPE) was included in the circuit model. When the exponent of the CPE approaches unity, the electrode surface behaves like an ideal capacitor; however, this is rarely achieved for pseudocapacitor material particularly.[134] The calculated CPE exponents were 0.82 for HRS and 0.78 for HSP, indicating that HRS is expected to possess higher pseudocapacitive surface activity.

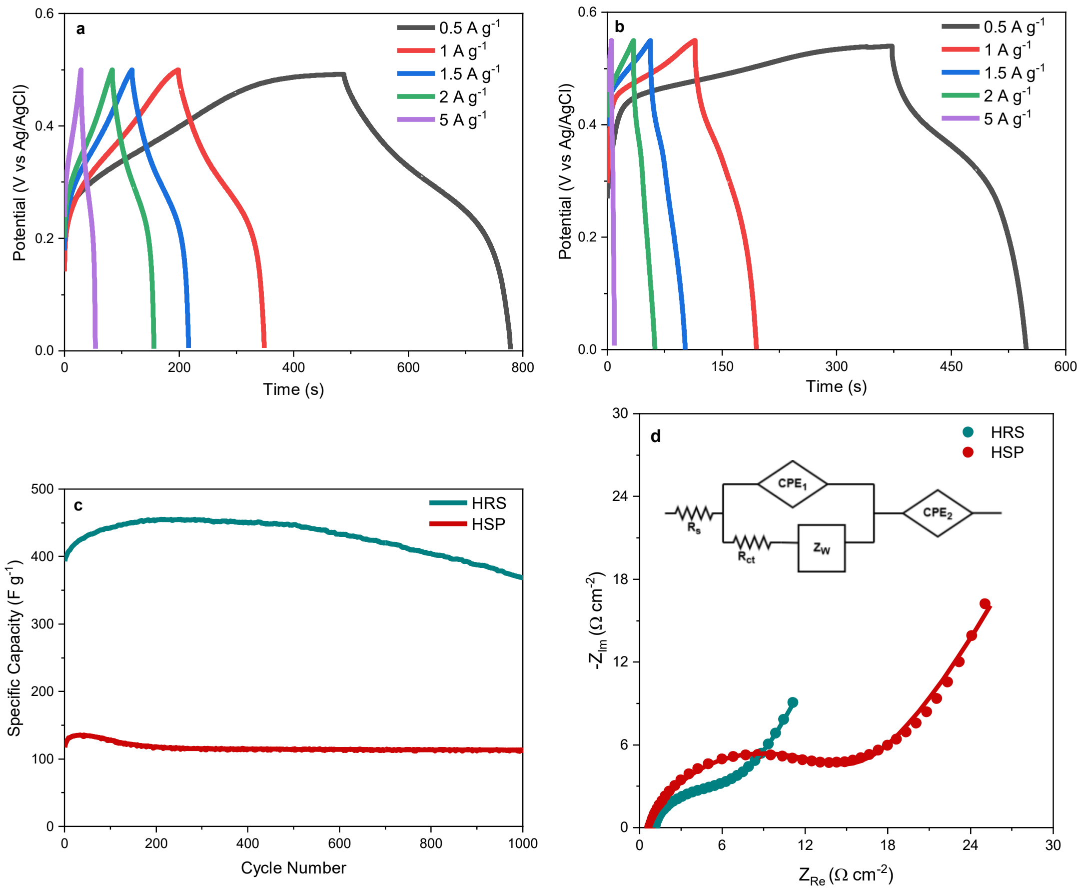

Figure 4.12 GCD results in three-electrode setup for (a) HRS and (b) HSP. (c) 1000-cycle GCD stability results in 2 A g^{-1}. (d) Fitted Nyquist diagrams of EIS experiment in three-electrode system.

After capacitive behavior analysis of the materials using three-electrode experiments, two-electrode tests were conducted to investigate supercapacitor device application, and results are shown in Fig. 4.13. Cyclic voltammogram of HRS-based asymmetric-supercapacitor and HSP-based asymmetric-supercapacitor are represented in Fig. 4.13a and Fig. 4.13b, respectively.

Device performance is evaluated based on calculated parameters of specific capacity, energy density, and power density from GCD results as shown in Fig. 4.13c and Fig. 4.13d for HRS and HSP, respectively. Specific capacities of the asymmetric supercapacitor (ASC), containing HRS as a positive electrode with negative carbon electrode, were calculated at current densities of 0.5, 1.0, 1.5, 2.0, and 5 A g^{-1} as 45.7, 36.6, 31.8, 27.9, and 15.2 F g^{-1}, respectively using the formula given in Eq. (40). Those for HSP were calculated as 31.5, 23.5, 12.4, 8.8, and 8.1 F g^{-1}. Energy and power densities were also calculated using Eq. (41) and Eq. (42), respectively. Energy densities were found to be 13.5, 10.3, 8.4, 7.0, and 2.5 Wh kg^{-1} at the same current densities, respectively for HRS. Those for HSP were calculated as 9.2, 6.4, 3.0, 1.9, and 1.6 Wh kg^{-1}. Lastly, power densities at the corresponding current densities were calculated as 365, 710, 1035, 1340, and 2750 W kg^{-1} for HRS and 363, 700, 990, 1240, and 2800 W kg^{-1} for HSP. Power and energy density values of both high entropy oxides are located in the boundaries of the asymmetric supercapacitor region on the Ragone plot as mentioned in literature review chapter.

EIS measurements were conducted for two-electrode case to investigate the mechanism of charge storage of the coin-cells with HRS and HSP electrodes as seen from Fig. 4.13e. Charge transfer resistances, R_{ct}, were calculated by EIS fitting as 6.2 Ω and 15.6 Ω for HRS and HSP, respectively. Both this and three-electrode results of EIS indicate that HRS accommodates charge transfer reactions on its surface easier than HSP because rock-salt structures usually are expected to have better electron mobility within the structure compared to spinel group as mentioned in the literature review chapter. The CPE exponents of HRS and HSP electrodes of coin-cells were calculated as 0.88 and 0.66, respectively. This result also is consistent with that of three-electrode EIS measurements. Warburg impedances also revealed as expected to be higher for HRS than HSP supporting the conclusion of surface-controlled and diffusion-controlled behavior of HRS and HSP, respectively.

Finally, the cyclic stability of the fabricated asymmetric supercapacitors was evaluated. As shown in Fig. 4.13f, the HRS-based device retained 75% of its maximum capacity after 1000 cycles at a current density of 2 A g^{-1}. In comparison, the HSP-based device maintained only 50% of its capacity under the same testing conditions. Overall, all these findings demonstrate that the HRS electrode exhibits superior stability compared to HSP, both in laboratory-scale zinc–air batteries and in asymmetric supercapacitor configurations.

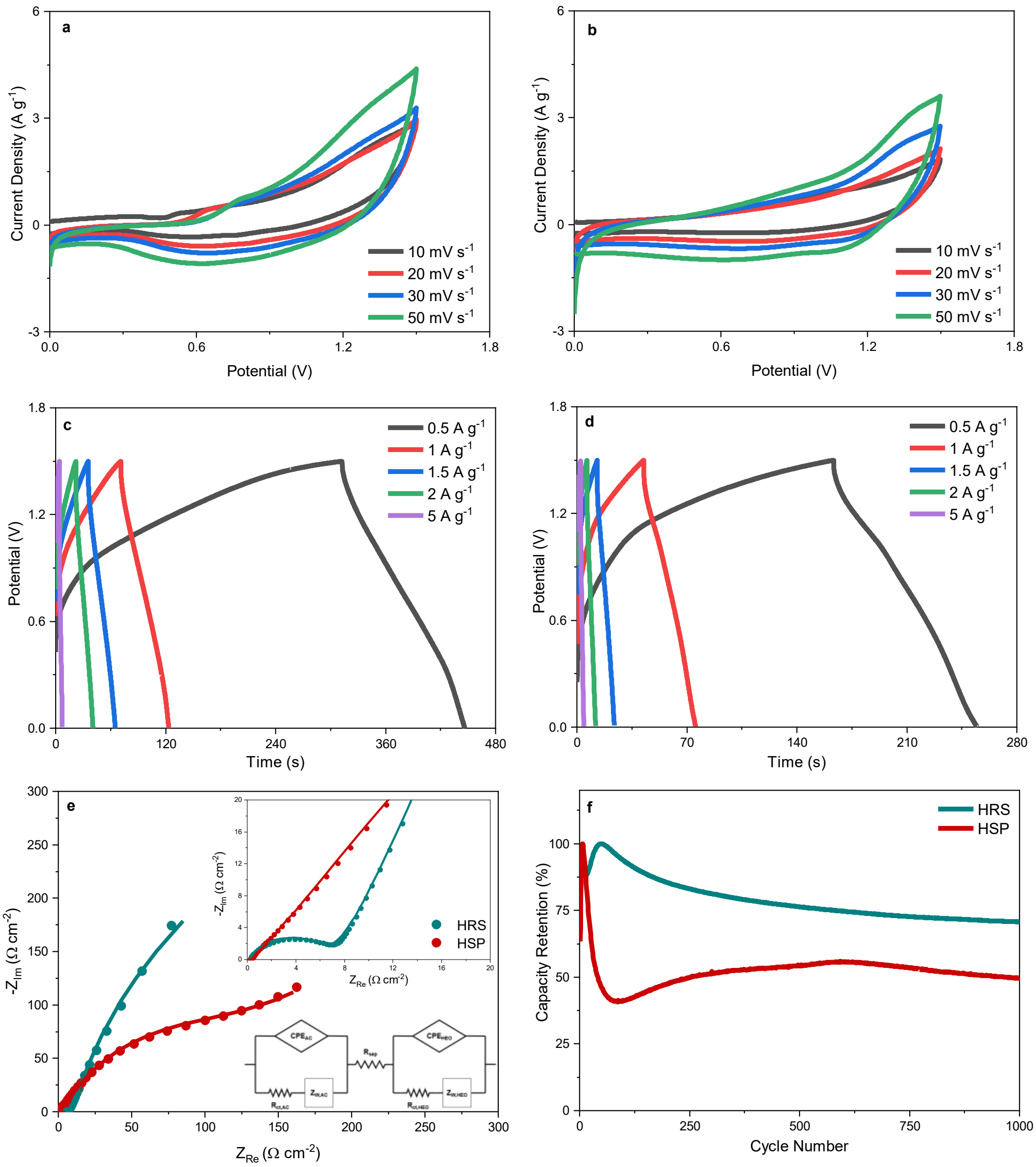

Figure 4.13 Asymmetric supercapacitor (CR2032) device tests: (a, b) CV curves for HRS and HSP, respectively; (c, d) GCD results for HRS and HSP, respectively; and (e) Nyquist plot for HRS and HSP.

CHAPTER 5

CONCLUSION

This study investigates crystal structure properties of rock-salt and spinel phases correlation with the performances of oxygen electrocatalyst for zinc-air battery and electrode materials for pseudocapacitor charge storage using basic structural modelling-refining approaches, and advanced experimental techniques along with the deep literature review.

- Two different high-entropy oxides were synthesized successfully with different heat treatments to obtain two distinct crystal phases, rock-salt and spinel, abbreviated as HRS and HSP, respectively.
- Each electrocatalyst exhibits its own distinctive structural characteristics owing to its crystal configuration. Analysis of XRD peak broadening using the Williamson-Hall method and Rietveld refinement by GSAS-II indicate that the rock-salt oxide (HRS) possesses a greater degree of microstrain when Co, Cr, Cu, Ni, and Al occupy the cationic sites. This finding is further supported by O1s spectral analysis, which suggests that the observed lattice distortion is primarily associated with the crystal structure itself rather than oxygen vacancies.
- HRS and HSP might be assumed to have similar theoretical configurational entropy due to the presence of five equimolar metal constituents at cationic sites, in addition to configurational entropy, microstrain contribution to stability can be considerably higher in HRS. As a result, HRS may be expected to exhibit enhanced cyclic stability compared to HSP, as confirmed by experimental observations. Consistent with this, cyclic charge–discharge measurements demonstrate that the HRS cathode retains stability for nearly 180 hours in zinc–air battery operation, while the HSP cathode, despite

showing slightly stronger bifunctional behavior, remains stable for only about 60 hours. Regarding catalytic performance.

- In terms of electrode characteristics, HRS was identified as a pseudocapacitive-type electrode, whereas HSP behaved as a battery-type electrode, as verified by both three-electrode and two-electrode setups.
- The capacitor performance of both electrode materials was evaluated, revealing that HRS exhibited higher specific capacitance than HSP, owing to its enhanced electrode activity as confirmed by electrochemical experiments.

REFERENCES

[1] Silva S, Soares I, Afonso O. Economic and environmental effects under resource scarcity and substitution between renewable and non-renewable resources. Energy Policy 2013;54:113–24. https://doi.org/10.1016/j.enpol.2012.10.069.

[2] Bogdanov D, Gulagi A, Fasihi M, Breyer C. Full energy sector transition towards 100% renewable energy supply: Integrating power, heat, transport and industry sectors including desalination. Appl Energy 2021;283:116273. https://doi.org/10.1016/j.apenergy.2020.116273.

[3] Akinyemi TO, Ramonu OJ. Mitigation of CO2 Emissions in Transportation and Industrial Processes using Renewable Energy Technologies. European Journal of Engineering and Technology Research 2019;4:58–66. https://doi.org/10.24018/ejeng.2019.4.5.1118.

[4] Owusu PA, Asumadu-Sarkodie S. A review of renewable energy sources, sustainability issues and climate change mitigation. Cogent Eng 2016;3:1167990. https://doi.org/10.1080/23311916.2016.1167990.

[5] Frate GF, Ferrari L, Desideri U. Energy storage for grid-scale applications: Technology review and economic feasibility analysis. Renew Energy 2021;163:1754–72. https://doi.org/10.1016/j.renene.2020.10.070.

[6] Zhu Z, Jiang T, Ali M, Meng Y, Jin Y, Cui Y, et al. Rechargeable Batteries for Grid Scale Energy Storage. Chem Rev 2022;122:16610–751. https://doi.org/10.1021/acs.chemrev.2c00289.

[7] Li Y, Gong M, Liang Y, Feng J, Kim J-E, Wang H, et al. Advanced zinc-air batteries based on high-performance hybrid electrocatalysts. Nat Commun 2013;4:1805. https://doi.org/10.1038/ncomms2812.

[8] Erdil T, Toparli C. B-Site Effect on High-Entropy Perovskite Oxide as a Bifunctional Electrocatalyst for Rechargeable Zinc–Air Batteries. ACS Appl Energy Mater 2023;6:11255–67. https://doi.org/10.1021/acsaem.3c02149.

[9] Katsounaros I, Cherevko S, Zeradjanin AR, Mayrhofer KJJ. Oxygen electrochemistry as a cornerstone for sustainable energy conversion. Angewandte Chemie - International Edition 2014;53:102–21. https://doi.org/10.1002/anie.201306588.

[10] Zeng K, Zhang D. Recent progress in alkaline water electrolysis for hydrogen production and applications. Prog Energy Combust Sci 2010;36:307–26. https://doi.org/10.1016/j.pecs.2009.11.002.

[11] ARAT HT, SÜRER MG. State of art of hydrogen usage as a fuel on aviation. European Mechanical Science 2017;2:20–30. https://doi.org/10.26701/ems.364286.

[12] Han N, Zhang W, Guo W, Pan H, Jiang B, Xing L, et al. Designing Oxide Catalysts for Oxygen Electrocatalysis: Insights from Mechanism to Application. Nanomicro Lett 2023;15:185. https://doi.org/10.1007/s40820-023-01152-z.

[13] Erdil T, Lokcu E, Yildiz I, Okuyucu C, Kalay YE, Toparli C. Facile Synthesis and Origin of Enhanced Electrochemical Oxygen Evolution Reaction Performance of 2H-Hexagonal $Ba_2CoMnO_{6-\delta}$ as a New Member in Double Perovskite Oxides. ACS Omega 2022;7:44147–55. https://doi.org/10.1021/acsomega.2c05627.

[14] Aamlid SS, Oudah M, Rottler J, Hallas AM. Understanding the Role of Entropy in High Entropy Oxides. J Am Chem Soc 2023;145:5991–6006. https://doi.org/10.1021/jacs.2c11608.

[15] Yin WJ, Weng B, Ge J, Sun Q, Li Z, Yan Y. Oxide perovskites, double perovskites and derivatives for electrocatalysis, photocatalysis, and

photovoltaics. Energy Environ Sci 2019;12:442–62. https://doi.org/10.1039/c8ee01574k.

[16] Wang X, Zuo Y, Horta S, He R, Yang L, Ostovari Moghaddam A, et al. CoFeNiMnZnB as a High-Entropy Metal Boride to Boost the Oxygen Evolution Reaction. ACS Appl Mater Interfaces 2022;14:48212–9. https://doi.org/10.1021/acsami.2c11627.

[17] Cui M, Yang C, Li B, Dong Q, Wu M, Hwang S, et al. High-Entropy Metal Sulfide Nanoparticles Promise High-Performance Oxygen Evolution Reaction. Adv Energy Mater 2021;11. https://doi.org/10.1002/aenm.202002887.

[18] Lai D, Kang Q, Gao F, Lu Q. High-entropy effect of a metal phosphide on enhanced overall water splitting performance. J Mater Chem A Mater 2021;9:17913–22. https://doi.org/10.1039/d1ta04755h.

[19] Xie X, Du L, Yan L, Park S, Qiu Y, Sokolowski J, et al. Oxygen Evolution Reaction in Alkaline Environment: Material Challenges and Solutions. Adv Funct Mater 2022;32. https://doi.org/10.1002/adfm.202110036.

[20] Pan Y, Liu J-X, Tu T-Z, Wang W, Zhang G-J. High-entropy oxides for catalysis: A diamond in the rough. Chemical Engineering Journal 2023;451:138659. https://doi.org/10.1016/j.cej.2022.138659.

[21] Huang Y, Wang D, Yu Y, Li Z, Wen X, Wang Z. High-Entropy Oxides as Electrocatalysts for the Oxygen Evolution Reaction: A Mini Review. Energy & Fuels 2024;38:13661–84. https://doi.org/10.1021/acs.energyfuels.4c02061.

[22] Bao W, Shen H, Zhang Y, Qian C, Zeng G, Jing K, et al. High-entropy oxides for energy storage and conversion. J Mater Chem A Mater 2024;12:23179–201. https://doi.org/10.1039/D4TA04156A.

[23] Raza W, Ali F, Raza N, Luo Y, Kim K-H, Yang J, et al. Recent advancements in supercapacitor technology. Nano Energy 2018;52:441–73. https://doi.org/10.1016/j.nanoen.2018.08.013.

[24] Dissanayake K, Kularatna-Abeywardana D. A review of supercapacitors: Materials, technology, challenges, and renewable energy applications. J Energy Storage 2024;96:112563. https://doi.org/10.1016/j.est.2024.112563.

[25] Chen G, Su Y, Kuang P, Liu Z, Chen D, Wu X, et al. Polypyrrole Shell@3D-Ni Metal Core Structured Electrodes for High-Performance Supercapacitors. Chemistry – A European Journal 2015;21:4614–21. https://doi.org/10.1002/chem.201405976.

[26] Niu B, Zhang F, Ping H, Li N, Zhou J, Lei L, et al. Sol-gel Autocombustion Synthesis of Nanocrystalline High-entropy Alloys. Sci Rep 2017;7:3421. https://doi.org/10.1038/s41598-017-03644-6.

[27] Rodríguez-Padrón D, Puente-Santiago AR, Balu AM, Muñoz-Batista MJ, Luque R. Environmental Catalysis: Present and Future. ChemCatChem 2019;11:18–38. https://doi.org/10.1002/cctc.201801248.

[28] Tu Q, Parvatker A, Garedew M, Harris C, Eckelman M, Zimmerman JB, et al. Electrocatalysis for Chemical and Fuel Production: Investigating Climate Change Mitigation Potential and Economic Feasibility. Environ Sci Technol 2021;55:3240–9. https://doi.org/10.1021/acs.est.0c07309.

[29] Li Y, Wang H, Priest C, Li S, Xu P, Wu G. Advanced Electrocatalysis for Energy and Environmental Sustainability via Water and Nitrogen Reactions. Advanced Materials 2021;33. https://doi.org/10.1002/adma.202000381.

[30] Ibrahim KB, Tsai M, Chala SA, Berihun MK, Kahsay AW, Berhe TA, et al. A review of transition metal-based bifunctional oxygen electrocatalysts. Journal of the Chinese Chemical Society 2019;66:829–65. https://doi.org/10.1002/jccs.201900001.

[31] Wang H, Tang C, Zhang Q. A Review of Precious-Metal-Free Bifunctional Oxygen Electrocatalysts: Rational Design and Applications in Zn−Air Batteries. Adv Funct Mater 2018;28. https://doi.org/10.1002/adfm.201803329.

[32] Yang H, Han X, Douka AI, Huang L, Gong L, Xia C, et al. Advanced Oxygen Electrocatalysis in Energy Conversion and Storage. Adv Funct Mater 2021;31. https://doi.org/10.1002/adfm.202007602.

[33] Katsounaros I, Cherevko S, Zeradjanin AR, Mayrhofer KJJ. Oxygen Electrochemistry as a Cornerstone for Sustainable Energy Conversion. Angewandte Chemie International Edition 2014;53:102–21. https://doi.org/10.1002/anie.201306588.

[34] Wang J, Wen J, Wang J, Yang B, Jiang L. Water electrolyzer operation scheduling for green hydrogen production: A review. Renewable and Sustainable Energy Reviews 2024;203:114779. https://doi.org/10.1016/j.rser.2024.114779.

[35] Qasem NAA, Abdulrahman GAQ. A Recent Comprehensive Review of Fuel Cells: History, Types, and Applications. Int J Energy Res 2024;2024. https://doi.org/10.1155/2024/7271748.

[36] Wang Z-L, Xu D, Xu J-J, Zhang X-B. Oxygen electrocatalysts in metal–air batteries: from aqueous to nonaqueous electrolytes. Chem Soc Rev 2014;43:7746–86. https://doi.org/10.1039/C3CS60248F.

[37] Du N, Roy C, Peach R, Turnbull M, Thiele S, Bock C. Anion-Exchange Membrane Water Electrolyzers. Chem Rev 2022;122:11830–95. https://doi.org/10.1021/acs.chemrev.1c00854.

[38] Blurton KF, Sammells AF. Metal/air batteries: Their status and potential — a review. J Power Sources 1979;4:263–79. https://doi.org/10.1016/0378-7753(79)80001-4.

[39] Liang Q, Brocks G, Bieberle-Hütter A. Oxygen evolution reaction (OER) mechanism under alkaline and acidic conditions. Journal of Physics: Energy 2021;3:026001. https://doi.org/10.1088/2515-7655/abdc85.

[40] Gong S, Zhang T, Meng J, Sun W, Tian Y. Advances in the mechanism investigation for the oxygen evolution reaction: fundamental theory and monitoring techniques. Mater Chem Front 2024;8:603–26. https://doi.org/10.1039/D3QM00935A.

[41] Xie X, Du L, Yan L, Park S, Qiu Y, Sokolowski J, et al. Oxygen Evolution Reaction in Alkaline Environment: Material Challenges and Solutions. Adv Funct Mater 2022;32. https://doi.org/10.1002/adfm.202110036.

[42] Choi S, Kim S-J, Han S, Wang J, Kim J, Koo B, et al. Enhancing Oxygen Evolution Reaction via a Surface Reconstruction-Induced Lattice Oxygen Mechanism. ACS Catal 2024;14:15096–107. https://doi.org/10.1021/acscatal.4c03594.

[43] Yoo JS, Rong X, Liu Y, Kolpak AM. Role of Lattice Oxygen Participation in Understanding Trends in the Oxygen Evolution Reaction on Perovskites. ACS Catal 2018;8:4628–36. https://doi.org/10.1021/acscatal.8b00612.

[44] Zhou B, Gao R, Zou J, Yang H. Surface Design Strategy of Catalysts for Water Electrolysis. Small 2022;18. https://doi.org/10.1002/smll.202202336.

[45] Goswami C, Hazarika KK, Bharali P. Transition metal oxide nanocatalysts for oxygen reduction reaction. Mater Sci Energy Technol 2018;1:117–28. https://doi.org/10.1016/j.mset.2018.06.005.

[46] Gao J, Liu B. Progress of Electrochemical Hydrogen Peroxide Synthesis over Single Atom Catalysts. ACS Mater Lett 2020;2:1008–24. https://doi.org/10.1021/acsmaterialslett.0c00189.

[47] Han J, Sun J, Chen S, Zhang S, Qi L, Husile A, et al. Structure–Activity Relationships in Oxygen Electrocatalysis. Advanced Materials 2024;36. https://doi.org/10.1002/adma.202408139.

[48] Wang Z-L, Xu D, Xu J-J, Zhang X-B. Oxygen electrocatalysts in metal–air batteries: from aqueous to nonaqueous electrolytes. Chem Soc Rev 2014;43:7746–86. https://doi.org/10.1039/C3CS60248F.

[49] McLean G. An assessment of alkaline fuel cell technology. Int J Hydrogen Energy 2002;27:507–26. https://doi.org/10.1016/S0360-3199(01)00181-1.

[50] Wang C, Yu Y, Niu J, Liu Y, Bridges D, Liu X, et al. Recent Progress of Metal–Air Batteries—A Mini Review. Applied Sciences 2019;9:2787. https://doi.org/10.3390/app9142787.

[51] Hu L, Xu X. Current Pulse-Based Measurement Technique for Zinc–Air Battery Parameters. Energies (Basel) 2023;16:6448. https://doi.org/10.3390/en16186448.

[52] Lee J, Tai Kim S, Cao R, Choi N, Liu M, Lee KT, et al. Metal–Air Batteries with High Energy Density: Li–Air versus Zn–Air. Adv Energy Mater 2011;1:34–50. https://doi.org/10.1002/aenm.201000010.

[53] Bi X, Jiang Y, Chen R, Du Y, Zheng Y, Yang R, et al. Rechargeable Zinc–Air versus Lithium–Air Battery: from Fundamental Promises Toward Technological Potentials. Adv Energy Mater 2024;14. https://doi.org/10.1002/aenm.202302388.

[54] Li Y, Dai H. Recent advances in zinc–air batteries. Chem Soc Rev 2014;43:5257–75. https://doi.org/10.1039/C4CS00015C.

[55] Nazir G, Rehman A, Lee J-H, Kim C-H, Gautam J, Heo K, et al. A Review of Rechargeable Zinc–Air Batteries: Recent Progress and Future Perspectives. Nanomicro Lett 2024;16:138. https://doi.org/10.1007/s40820-024-01328-1.

[56] Shabeer Y, Madani SS, Panchal S, Mousavi M, Fowler M. Different Metal–Air Batteries as Range Extenders for the Electric Vehicle Market: A Comparative Study. Batteries 2025;11:35. https://doi.org/10.3390/batteries11010035.

[57] Hosseini S, Masoudi Soltani S, Li Y-Y. Current status and technical challenges of electrolytes in zinc–air batteries: An in-depth review. Chemical Engineering Journal 2021;408:127241. https://doi.org/10.1016/j.cej.2020.127241.

[58] Caramia V, Bozzini B. Materials science aspects of zinc–air batteries: a review. Mater Renew Sustain Energy 2014;3:28. https://doi.org/10.1007/s40243-014-0028-3.

[59] Winter M, Brodd RJ. What Are Batteries, Fuel Cells, and Supercapacitors? Chem Rev 2004;104:4245–70. https://doi.org/10.1021/cr020730k.

[60] Shao Y, El-Kady MF, Sun J, Li Y, Zhang Q, Zhu M, et al. Design and Mechanisms of Asymmetric Supercapacitors. Chem Rev 2018;118:9233–80. https://doi.org/10.1021/acs.chemrev.8b00252.

[61] Nilsson JWilliam, Riedel SA. Electric circuits. Pearson; 2015.

[62] Sharma P, Bhatti TS. A review on electrochemical double-layer capacitors. Energy Convers Manag 2010;51:2901–12. https://doi.org/10.1016/j.enconman.2010.06.031.

[63] Banerjee S, Mordina B, Sinha P, Kar KK. Recent advancement of supercapacitors: A current era of supercapacitor devices through the development of electrical double layer, pseudo and their hybrid supercapacitor electrodes. J Energy Storage 2025;108:115075. https://doi.org/10.1016/j.est.2024.115075.

[64] Yang S, Wang S, Liu X, Li L. Biomass derived interconnected hierarchical micro-meso-macro- porous carbon with ultrahigh capacitance for

supercapacitors. Carbon N Y 2019;147:540–9. https://doi.org/10.1016/j.carbon.2019.03.023.

[65] Seenivasan S, Adhikari S, Sivagurunathan AT, Kim D-H. Supercapatteries: unlocking the potential of battery-supercapacitor fusion. Energy Environ Sci 2025;18:1054–95. https://doi.org/10.1039/D4EE04348K.

[66] Seenivasan S, Adhikari S, Sivagurunathan AT, Kim D-H. Supercapatteries: unlocking the potential of battery-supercapacitor fusion. Energy Environ Sci 2025;18:1054–95. https://doi.org/10.1039/D4EE04348K.

[67] Kumar N, Kim S-B, Lee S-Y, Park S-J. Recent Advanced Supercapacitor: A Review of Storage Mechanisms, Electrode Materials, Modification, and Perspectives. Nanomaterials 2022;12:3708. https://doi.org/10.3390/nano12203708.

[68] Lakshmi KCS, Vedhanarayanan B. High-Performance Supercapacitors: A Comprehensive Review on Paradigm Shift of Conventional Energy Storage Devices. Batteries 2023;9:202. https://doi.org/10.3390/batteries9040202.

[69] An C, Zhang Y, Guo H, Wang Y. Metal oxide-based supercapacitors: progress and prospectives. Nanoscale Adv 2019;1:4644–58. https://doi.org/10.1039/C9NA00543A.

[70] Augustyn V, Simon P, Dunn B. Pseudocapacitive oxide materials for high-rate electrochemical energy storage. Energy Environ Sci 2014;7:1597. https://doi.org/10.1039/c3ee44164d.

[71] Liu Y, Jiang SP, Shao Z. Intercalation pseudocapacitance in electrochemical energy storage: recent advances in fundamental understanding and materials development. Mater Today Adv 2020;7:100072. https://doi.org/10.1016/j.mtadv.2020.100072.

[72] Liu Y, Zhu Z, Wu J, Wang Z, Zhang H, Xu Y, et al. Tuning crystal structure and electronic properties for enhanced oxygen intercalation

pseudocapacitance in perovskite. Cell Rep Phys Sci 2024;5:101846. https://doi.org/10.1016/j.xcrp.2024.101846.

[73] Sharma S, Chand P. Supercapacitor and electrochemical techniques: A brief review. Results Chem 2023;5:100885. https://doi.org/10.1016/j.rechem.2023.100885.

[74] Hussain I, Lamiel C, Ahmad M, Chen Y, Shuang S, Javed MS, et al. High entropy alloys as electrode material for supercapacitors: A review. J Energy Storage 2021;44:103405. https://doi.org/10.1016/j.est.2021.103405.

[75] George J, Balachandran M. Extrinsic pseudocapacitance: Tapering the borderline between pseudocapacitive and battery type electrode materials for energy storage applications. J Energy Storage 2023;74:109292. https://doi.org/10.1016/j.est.2023.109292.

[76] He X, Zhang X. A comprehensive review of supercapacitors: Properties, electrodes, electrolytes and thermal management systems based on phase change materials. J Energy Storage 2022;56:106023. https://doi.org/10.1016/j.est.2022.106023.

[77] Feng L, Yang P, Ling W, Wang S, Shi J, Wang F. 3D hierarchical flower-like NiMoO4@Ni3S2 composites on Ni foam for high-performance battery-type supercapacitors. Journal of Physics and Chemistry of Solids 2021;148:109697. https://doi.org/10.1016/j.jpcs.2020.109697.

[78] Guo M, Liu Y, Zhang F, Cheng F, Cheng C, Miao Y, et al. Inactive Al3+-doped La(CoCrFeMnNiAlx)1/(5+x)O3 high-entropy perovskite oxides as high performance supercapacitor electrodes. Journal of Advanced Ceramics 2022;11:742–53. https://doi.org/10.1007/s40145-022-0568-4.

[79] Bora M, Bhattacharjya D, Saikia BK. Coal-Derived Activated Carbon for Electrochemical Energy Storage: Status on Supercapacitor, Li-Ion Battery, and Li–S Battery Applications. Energy & Fuels 2021;35:18285–307. https://doi.org/10.1021/acs.energyfuels.1c02518.

[80] Zhang J, Gu M, Chen X. Supercapacitors for renewable energy applications: A review. Micro and Nano Engineering 2023;21:100229. https://doi.org/10.1016/j.mne.2023.100229.

[81] Muzaffar A, Ahamed MB, Hussain CM. Green supercapacitors: Latest developments and perspectives in the pursuit of sustainability. Renewable and Sustainable Energy Reviews 2024;195:114324. https://doi.org/10.1016/j.rser.2024.114324.

[82] Park HW, Roh KC. Recent advances in and perspectives on pseudocapacitive materials for Supercapacitors–A review. J Power Sources 2023;557:232558. https://doi.org/10.1016/j.jpowsour.2022.232558.

[83] Khalid M. A Review on the Selected Applications of Battery-Supercapacitor Hybrid Energy Storage Systems for Microgrids. Energies (Basel) 2019;12:4559. https://doi.org/10.3390/en12234559.

[84] Fathabadi H. Novel fuel cell/battery/supercapacitor hybrid power source for fuel cell hybrid electric vehicles. Energy 2018;143:467–77. https://doi.org/10.1016/j.energy.2017.10.107.

[85] Aamlid SS, Oudah M, Rottler J, Hallas AM. Understanding the Role of Entropy in High Entropy Oxides. J Am Chem Soc 2023;145:5991–6006. https://doi.org/10.1021/jacs.2c11608.

[86] Hsu W-L, Tsai C-W, Yeh A-C, Yeh J-W. Clarifying the four core effects of high-entropy materials. Nat Rev Chem 2024;8:471–85. https://doi.org/10.1038/s41570-024-00602-5.

[87] Huo X, Yu H, Xing B, Zuo X, Zhang N. Review of High Entropy Alloys Electrocatalysts for Hydrogen Evolution, Oxygen Evolution, and Oxygen Reduction Reaction. The Chemical Record 2022;22. https://doi.org/10.1002/tcr.202200175.

[88] Schweidler S, Botros M, Strauss F, Wang Q, Ma Y, Velasco L, et al. High-entropy materials for energy and electronic applications. Nat Rev Mater 2024;9:266–81. https://doi.org/10.1038/s41578-024-00654-5.

[89] Albedwawi SH, AlJaberi A, Haidemenopoulos GN, Polychronopoulou K. High entropy oxides-exploring a paradigm of promising catalysts: A review. Mater Des 2021;202:109534. https://doi.org/10.1016/j.matdes.2021.109534.

[90] Sarkar A, Wang Q, Schiele A, Chellali MR, Bhattacharya SS, Wang D, et al. High-Entropy Oxides: Fundamental Aspects and Electrochemical Properties. Advanced Materials 2019;31. https://doi.org/10.1002/adma.201806236.

[91] Fu M, Ma X, Zhao K, Li X, Su D. High-entropy materials for energy-related applications. IScience 2021;24:102177. https://doi.org/10.1016/j.isci.

[92] Liu Z-Y, Liu Y, Xu Y, Zhang H, Shao Z, Wang Z, et al. Novel high-entropy oxides for energy storage and conversion: From fundamentals to practical applications. Green Energy & Environment 2023;8:1341–57. https://doi.org/10.1016/j.gee.2023.04.007.

[93] Lökçü E, Anik M. Investigating the Structural and Lithium Storage Properties of High-Entropy Oxides in the Mg-Co-Ni-Cu-Zn-O System. Scr Mater 2024;240:115840. https://doi.org/10.1016/j.scriptamat.2023.115840.

[94] Shao L, Jiang H, Xu C, Ding N, Tang B-Y. The lattice distortion, mechanical and thermodynamic properties of A(Zr0.2Sn0.2Ti0.2Hf0.2Nb0.2)O3 (A = Sr, Ba) high-entropy perovskite with B-site disorder: First principles prediction. Mater Des 2022;224:111308. https://doi.org/10.1016/j.matdes.2022.111308.

[95] Li J. Oxygen Evolution Reaction in Energy Conversion and Storage: Design Strategies Under and Beyond the Energy Scaling Relationship. Nanomicro Lett 2022;14:112. https://doi.org/10.1007/s40820-022-00857-x.

[96] Hou Z, Cui C, Li Y, Gao Y, Zhu D, Gu Y, et al. Lattice-Strain Engineering for Heterogenous Electrocatalytic Oxygen Evolution Reaction. Advanced Materials 2023;35. https://doi.org/10.1002/adma.202209876.

[97] Wu H, Lu Q, Li Y, Zhao M, Wang J, Li Y, et al. Structural Framework-Guided Universal Design of High-Entropy Compounds for Efficient Energy Catalysis. J Am Chem Soc 2023;145:1924–35. https://doi.org/10.1021/jacs.2c12295.

[98] Song H, Tian F, Hu Q-M, Vitos L, Wang Y, Shen J, et al. Local lattice distortion in high-entropy alloys. Phys Rev Mater 2017;1:023404. https://doi.org/10.1103/PhysRevMaterials.1.023404.

[99] Baek J, Hossain MD, Mukherjee P, Lee J, Winther KT, Leem J, et al. Synergistic effects of mixing and strain in high entropy spinel oxides for oxygen evolution reaction. Nat Commun 2023;14:5936. https://doi.org/10.1038/s41467-023-41359-7.

[100] Li X, Sun Y, Ren F, Bai Y, Cheng Z. Smart oxygen vacancy engineering to enhance water oxidation efficiency by separating the different effects of bulk and surface vacancies. Mater Today Energy 2021;19:100619. https://doi.org/10.1016/j.mtener.2020.100619.

[101] Ji Q, Bi L, Zhang J, Cao H, Zhao XS. The role of oxygen vacancies of ABO_3 perovskite oxides in the oxygen reduction reaction. Energy Environ Sci 2020;13:1408–28. https://doi.org/10.1039/D0EE00092B.

[102] Ozgur C, Erdil T, Geyikci U, Okuyucu C, Lokcu E, Kalay YE, et al. Engineering Oxygen Vacancies in $(FeCrCoMnZn)_3O_{4-\delta}$ High Entropy Spinel Oxides Through Altering Fabrication Atmosphere for High-Performance Rechargeable Zinc-Air Batteries. Global Challenges 2024;8. https://doi.org/10.1002/gch2.202300199.

[103] Hu X, Wan C, Tang A, Ju X. Controllable nitrogen-doped carbon layers coated on NiCoO2 as electrodes for high-performance hybrid

supercapacitors. Appl Surf Sci 2021;569:150924. https://doi.org/10.1016/j.apsusc.2021.150924.

[104] Sun X, Sun J, Guo L, Hou L, Yuan C. Understanding the crystal structure-dependent electrochemical capacitance of spinel and rock-salt Ni–Co oxides *via* density function theory calculations. RSC Adv 2020;10:35611–8. https://doi.org/10.1039/D0RA05578F.

[105] Wang J, Zhao C-X, Liu J-N, Ren D, Li B-Q, Huang J-Q, et al. Quantitative kinetic analysis on oxygen reduction reaction: A perspective. Nano Materials Science 2021;3:313–8. https://doi.org/10.1016/j.nanoms.2021.03.006.

[106] Wei C, Rao RR, Peng J, Huang B, Stephens IEL, Risch M, et al. Recommended Practices and Benchmark Activity for Hydrogen and Oxygen Electrocatalysis in Water Splitting and Fuel Cells. Advanced Materials 2019;31. https://doi.org/10.1002/adma.201806296.

[107] Wei L-Z, Shi S-J, Guo M-Y, Guo R-F, Shen P. Self-supporting high-entropy-oxide@layered-Ni electrode for high-performance supercapacitors. J Energy Storage 2025;110:115351. https://doi.org/10.1016/j.est.2025.115351.

[108] R AS, Jacob G. Exploring the charge storage ability of the spinel-type high entropy oxide (MnFeCoNiZn)3O4 nanoparticles for supercapacitor applications. Chemical Engineering Journal Advances 2025;21:100708. https://doi.org/10.1016/j.ceja.2025.100708.

[109] Coskuner AB, Erdil T, Ozgur C, Geyikci U, Toparli C. Tuning the lattice strain through manipulating crystal structure of high entropy oxides enhances electrocatalytic performance. Mater Res Bull 2025;186:113333. https://doi.org/10.1016/j.materresbull.2025.113333.

[110] Lee M. X-RAY DIFFRACTION FOR MATERIALS RESEARCH From Fundamentals to Applications. n.d.

[111] ’Lee M. X-Ray diffraction for materials research: from fundamentals to applications. CRC Press; 2016.

[112] Musicó BL. Synthesis and Physical Properties of High Entropy Oxide Synthesis and Physical Properties of High Entropy Oxide Ceramics Ceramics. n.d.

[113] Laïk B, Richet M, Emery N, Bach S, Perrière L, Cotrebil Y, et al. XPS Investigation of Co–Ni Oxidized Compounds Surface Using Peak-On-Satellite Ratio. Application to Co $_{20}$ Ni $_{80}$ Passive Layer Structure and Composition. ACS Omega 2024;9:40707–22. https://doi.org/10.1021/acsomega.4c05082.

[114] Lee KB, Jo S, Choi H, Lee Y-W, Sohn JI. Boosting catalyst activity with high valency metal species through Fe doping on normal spinel NiCr2O4 for superior water oxidation. Appl Surf Sci 2023;609:155326. https://doi.org/10.1016/j.apsusc.2022.155326.

[115] Usharani NJ, Shringi R, Sanghavi H, Subramanian S, Bhattacharya SS. Role of size, alio-/multi-valency and non-stoichiometry in the synthesis of phase-pure high entropy oxide (Co,Cu,Mg,Na,Ni,Zn)O. Dalton Transactions 2020;49:7123–32. https://doi.org/10.1039/D0DT00958J.

[116] Toparli C, Sarfraz A, Wieck AD, Rohwerder M, Erbe A. In situ and operando observation of surface oxides during oxygen evolution reaction on copper. Electrochim Acta 2017;236:104–15. https://doi.org/10.1016/j.electacta.2017.03.137.

[117] Toparli C, Sarfraz A, Erbe A. A new look at oxide formation at the copper/electrolyte interface by in situ spectroscopies. Physical Chemistry Chemical Physics 2015;17:31670–9. https://doi.org/10.1039/C5CP05172J.

[118] Lai D, Ling L, Su M, Kang Q, Gao F, Lu Q. From amorphous to crystalline: a universal strategy for structure regulation of high-entropy transition metal oxides. Chem Sci 2023;14:1787–96. https://doi.org/10.1039/D2SC04900G.

[119] Walsh A, Butler KT. Prediction of Electron Energies in Metal Oxides. Acc Chem Res 2014;47:364–72. https://doi.org/10.1021/ar400115x.

[120] Zhang X, Liu T, Zhu L, Guan J, Lu Y, Keal TW, et al. Bulk and Surface Contributions to Ionisation Potentials of Metal Oxides. Angewandte Chemie International Edition 2023;62. https://doi.org/10.1002/anie.202308411.

[121] Noguera C. Clean Oxide Surfaces: a theoretical review, 2001, p. 35–93. https://doi.org/10.1016/S1571-0785(01)80022-5.

[122] Pawlak DA, Ito M, Oku M, Shimamura K, Fukuda T. Interpretation of XPS O (1s) in Mixed Oxides Proved on Mixed Perovskite Crystals. J Phys Chem B 2002;106:504–7. https://doi.org/10.1021/jp012040a.

[123] Barr TL. Modern ESCA. CRC Press; 2020. https://doi.org/10.1201/9781003069041.

[124] Chen C, Su H, Lu L-N, Hong Y-S, Chen Y, Xiao K, et al. Interfacing spinel NiCo2O4 and NiCo alloy derived N-doped carbon nanotubes for enhanced oxygen electrocatalysis. Chemical Engineering Journal 2021;408:127814. https://doi.org/10.1016/j.cej.2020.127814.

[125] Bredar ARC, Chown AL, Burton AR, Farnum BH. Electrochemical Impedance Spectroscopy of Metal Oxide Electrodes for Energy Applications. ACS Appl Energy Mater 2020;3:66–98. https://doi.org/10.1021/acsaem.9b01965.

[126] Morales DM, Risch M. Seven steps to reliable cyclic voltammetry measurements for the determination of double layer capacitance. Journal of Physics: Energy 2021;3:034013. https://doi.org/10.1088/2515-7655/abee33.

[127] Ge X, Sumboja A, Wuu D, An T, Li B, Goh FWT, et al. Oxygen Reduction in Alkaline Media: From Mechanisms to Recent Advances of Catalysts. ACS Catal 2015;5:4643–67. https://doi.org/10.1021/acscatal.5b00524.

[128] Wei L-Z, Shi S-J, Guo M-Y, Guo R-F, Shen P. Self-supporting high-entropy-oxide@layered-Ni electrode for high-performance supercapacitors. J Energy Storage 2025;110:115351. https://doi.org/10.1016/j.est.2025.115351.

[129] Pholauyphon W, Charoen-amornkitt P, Suzuki T, Tsushima S. Perspectives on accurately analyzing cyclic voltammograms for surface- and diffusion-controlled contributions. Electrochem Commun 2024;159:107654. https://doi.org/10.1016/j.elecom.2023.107654.

[130] Liu T -C., Pell WG, Conway BE, Roberson SL. Behavior of Molybdenum Nitrides as Materials for Electrochemical Capacitors: Comparison with Ruthenium Oxide. J Electrochem Soc 1998;145:1882–8. https://doi.org/10.1149/1.1838571.

[131] Sunil V, Pal B, Izwan Misnon I, Jose R. Characterization of supercapacitive charge storage device using electrochemical impedance spectroscopy. Mater Today Proc 2021;46:1588–94. https://doi.org/10.1016/j.matpr.2020.07.248.

[132] Qu D, Wang G, Kafle J, Harris J, Crain L, Jin Z, et al. Electrochemical Impedance and its Applications in Energy-Storage Systems. Small Methods 2018;2. https://doi.org/10.1002/smtd.201700342.

[133] Bard AJ; FLR. ELECTROCHEMICAL METHODS Fundamentals and Applications. 2nd ed. 2001.

[134] Magar HS, Hassan RYA, Mulchandani A. Electrochemical Impedance Spectroscopy (EIS): Principles, Construction, and Biosensing Applications. Sensors 2021;21:6578. https://doi.org/10.3390/s21196578.